UNIVERSITY OF OKLAHOMA

GRADUATE COLLEGE

CO_2 HUFF-N-PUFF IN UNCONVENTIONAL RESOURCES PLAYS – AN INTEGRATED MODELING APPROACH FOCUSING ON PERMIAN BASIN

A THESIS

SUBMITTED TO THE GRADUATE FACULTY

in partial fulfillment of the requirements for the

Degree of

MASTER OF SCIENCE

By

TIEN N. PHAN
Norman, Oklahoma
2019

Downloaded from SHAREOK. Persistent Handle URL: https://hdl.handle.net/11244/321088

CO_2 HUFF-N-PUFF IN UNCONVENTIONAL RESOURCES PLAYS – AN INTEGRATED MODELING APPROACH FOCUSING ON PERMIAN BASIN

A THESIS APPROVED FOR THE
MEWBOURNE SCHOOL OF PETROLEUM AND GEOLOGICAL ENGINEERING

BY

Dr. Zulfiquar Reza, Chair

Dr. Deepak Devegowda

Dr. John Pigott

© Copyright by TIEN N. PHAN 2019
All Rights Reserved.

Acknowledgements

I would sincerely like to thank my advisor, Dr. Zulfiquar Reza for his help and constant support throughout my graduate program at the University of Oklahoma. His advices, guidance, and motivation make it possible for me to complete my degree. I was very fortunate to learn and receive from his extensive industry and research experience. I am also very grateful for his patience and dedication on mentoring me in research work and publishing manuscripts.

I would also like to thank Dr. Deepak Devegowda and Dr. John Pigott, for their participating in my committee and providing valuable suggestions and feedbacks for my thesis.

Many thanks to my research teammates, Yuliana Zapata, Any Ordonez, Yao Wang and Tarek Mohammed for sharing, help and being friendly. Special thanks to Yuliana Zapata for collaborating in publishing manuscripts.

I would like to give a special thanks to my spouse Nhung Ha for always being with me, endless love, incredible support and encouragement.

Finally, I would like to deepest express my gratitude to my loved family. Special thanks to my mom E Le for taking care of my little son during the difficult times.

Table of Contents

Acknowledgements iv

List of Tables vii

List of Figures viii

Abstract xi

Chapter 1: Introduction and Objective 1

1.1 Introduction 1

1.2 Objective 2

1.3 Thesis Organization 3

Chapter 2: Integrated Modeling in Unconventional Reservoirs 5

2.1 Geological and Mechanical Earth Models 5

2.1.1 Geological Model 5

2.1.1 Mechanical Earth Model 10

2.2 Hydraulic-Fracture Modeling 13

2.2.1. Main Hydraulic Fracturing Model Inputs 14

2.2.2. Pumping Schedule and Design 15

2.2.3. Modeling Hydraulic-Fracture Geometries and Network 16

2.3 Reservoir Settings and Dynamic Model 18

2.3.1 Static Model 18

2.3.2 Compositional Fluids and Rock Physics 18

2.3.3 Well Model 21

2.3.4 Reservoir-Model Settings 21

2.3.5 Huff-n-Puff Processes 23

Chapter 3: Molecular Diffusion Models 24
3.1 Liquid-Phase Diffusion 25
3.2 Gas-Phase Diffusion 26
3.3 Pressure and Temperature Sensitivity to Diffusion Coefficients 26
3.4 Lumped-Component Diffusion Coefficients 28
Chapter 4: CO_2 Huff-n-Puff Reservoir Simulation 30
4.1 CO_2 Huff-n-Puff Diffusion Incremental Recovery 31
4.2 Sensitivity in Reservoir Quality 36
4.3 Sensitivity in Diffusion Coefficient 38
Chapter 5: Compositional Variation 40
5.1 Variation in Thermophysical Properties 40
5.2 Contacted CO_2 Volumes and CO_2 Retention in the Porous Media 48
Chapter 6: Discussions, Limitations and Future Work 51
Chapter 7: Conclusions 54
Nomenclature 56
References 57
Appendix 60
A1. Additional Figures 60
A2. Minimum Miscibility Pressure (MMP) Correlations 63

List of Tables

Table 1. Minimum and maximum values of the major petrophysical, mineralogical and variogram inputs employed in Design of Experiment (DoE). 10

Table 2. Hydraulic-fracturing design parameters used in this study. 14

Table 3. Simulated hydraulic-fracture network for the base case model. 17

Table 4. Basic reservoir settings for the base-case reservoir model. 18

Table 5. Lumped composition for in-situ liquid-rich oil unconventional reservoir. 19

Table 6. Inputs for rock physics model used in shale system. 20

Table 7. Lennard-Jones potential parameters for the components. 26

Table 8. Liquid-phase diffusion coefficients at three different pressures. 28

Table 9. Gas-phase diffusion coefficients at different pressures. 29

Table 10. Simulation cases description. 31

Table 11. Normalized C_{5+} mole fraction for MMP model. 34

Table 12. MMP Results Using Various Correlations 35

Table 13. Incremental oil recovery for cases at different reservoir qualities. 37

Table 14. Variation in production (lb-mole) for different diffusion-coefficients cases. 39

List of Figures

Figure 1. U.S. oil production from major shale plays (Modified from EIA, 2018). 1

Figure 2. Wolfcamp structure map with well locations of study area. 5

Figure 3. Study Area in the Midland Basin and stratigraphy column (modified from Fu, 2015). 6

Figure 4. 3D static model encompasses upper and lower of Wolfcamp formations with horizontal well landing in Wolfcamp A. 6

Figure 5. 3D facies model with horizontal well landing in Wolfcamp A formation. 7

Figure 6. Facies log and available logs 8

Figure 7. 3D porosity model with horizontal well landing in Wolfcamp A formation. 9

Figure 8. 3D permeability model with horizontal well landing in Wolfcamp A formation. 9

Figure 9. Principal geomechanical properties derived from sonic and other logs (last 3 tracks on the right side). 11

Figure 10. Strong correlation between Vp and Vs with distinct separation among limestone, dolomite and clean sandstone (from Castagna et al., 2014). 12

Figure 11. 3D Young's Modulus and Poisson's Ratio from various realizations of mineralogical and geological inputs. 13

Figure 12. Plug-and-perf hydraulic-fracturing schedule used in this study. 16

Figure 13. Example of resulting multi-stage hydraulic-fracture network from the base-case reservoir model. 17

Figure 14. Compositional lumping by different PVT techniques 19

Figure 15. Relative permeability curves for typical shales formation (from Ojha et al., 2017) in (a) and generated relative permeability curves used in this study in (b). 20

Figure 16. Definition of 4 distinct reservoir partitions of the stimulated regions surrounding hydraulically fractured well. 22
Figure 17. Well scheduling of CO_2 cyclic injection process. 23
Figure 18. Proposed workflow of diffusion coefficients method used in this study. 25
Figure 19. Diffusion coefficients variation with pressure and temperature..... 27
Figure 20. Well-performance comparison between diffusion and without diffusion. 32
Figure 21. Comparison of CO_2 distribution in matrix and natural fracture between diffusion and no diffusion effect. 33
Figure 22. MMP estimation using Holm and Josendal method (modified from Jarrell et al., 2012) 34
Figure 23. Huff-n-puff simulation results of different scenarios of reservoir quality and diffusion. 36
Figure 24. Component production stream (CO_2, C_{7+}) comparison for different reservoir quality cases. 37
Figure 25. Component-production stream (CO_2, C_{7+}) comparison for different diffusion-coefficients cases. 39
Figure 26. Evolution of total CO_2 mole fraction through selected injection cycles (SRV Region 1 only). 41
Figure 27. Evolution of CO_2 total mole-fraction through selected injection cycles (all SRV regions). 42
Figure 28. Evolution of liquid C_{7+} mole fraction through selected injection cycles (all SRV regions). 43

Figure 29. Evolution of methane total mole fraction through selected injection cycles (all SRV regions). 44
Figure 30. Evolution of pressure variation over through selected injection cycles (all SRV regions). 45
Figure 31. Evolution of reduction in oil saturation through selected injection cycles (all SRV regions). 46
Figure 32. Evolution of oil viscosity reduction through selected injection cycles (all SRV regions). 47
Figure 33. Evolution of oil-vapor surface tension through selected injection cycles (all SRV regions). 48
Figure 34. CO_2 diffusion efficiency into the rock matrix of the SRV. 49
Figure 35. CO_2 retention rate through huff-n-puff injection. Diffusion captures more CO_2 retained in the rock matrix 50
Figure 36. Component production stream (C_1, C_2-C_4, and C_5-C_7) comparison for different reservoir quality cases with diffusion effect. 60
Figure 37. Component production stream (CO_2, C_{7+}, C_1, C_2-C_4, and C_5-C_7) comparison for different reservoir quality cases without diffusion effect. 61
Figure 38. Pressure variation around the near wellbore regions through CO_2 huff-n-puff cycles 62

Abstract

Despite the recent growth in oil production from unconventional reservoirs, existing hydraulically fractured horizontal wells face challenges of poor recovery with the rapid production decline over a short life span. Enhanced recovery techniques, such as CO_2 huff-n-puff can be a solution to this impending problem and lead to energy independence for the foreseeable future. However, mechanisms occurring around the hydraulically fractured wells are far from fully understood. The primary motivation of this study revolves around addressing this limitation. Specifically, this study explored the evolution of various thermophysical properties occurring around hydraulically fractured wells in liquid-rich unconventional reservoirs using a holistic, integrated modeling framework.

Available well-logs and other data from Howard County in the Midland Basin formed the basis for constructing representative 3D structural models that capture the Midland Basin stratigraphy. A fracture simulator was used to create multistage hydraulic fractures that were integrated into numerical reservoir-flow simulation models. Then, both convective and diffusive flow within a multicomponent compositional simulation modeling paradigm is used to examine the role of molecular diffusion in performance under cyclic CO_2 injections in hydraulically fractured well. The simulation results indicate that molecular diffusion yields an incremental oil recovery of 6% compared to models that do not. Thorough analysis reveals different thermophysical properties transition from near wellbore regions to outer regions into the rock matrix. Changes in total mole fractions of CO_2, methane, and hydrocarbons with C_{7+} fraction, pressure and saturation variation, viscosity reduction and the surface tension over 14 injection-soaking-production cycles are tracked. The analyses of the evolution of these thermophysical properties provide the means to

evaluate the efficiency of the solvent injection process. The simulation results explain how, when, and where CO_2 disperses into the reservoir.

Chapter 1: Introduction and Objective

1.1 Introduction

Major shale oil plays are driving the growth of U.S. crude oil outputs in recent years. From 2016 to 2018, unconventional plays contributed to approximately 90% of oil production growth in the U.S. In particular, the Permian Basin will account for more than half of the growth in crude oil production through 2019 (**Figure 1**, EIA, 2018). In addition, advances in hydraulic fracturing and completion techniques in recent years have played dominant roles in unlocking the potentials of vast U.S. shale resources (Hoffman, 2018). Operators and service companies are continually developing innovative completions, fracturing, and well-spacing techniques to maximize production in these reservoirs.

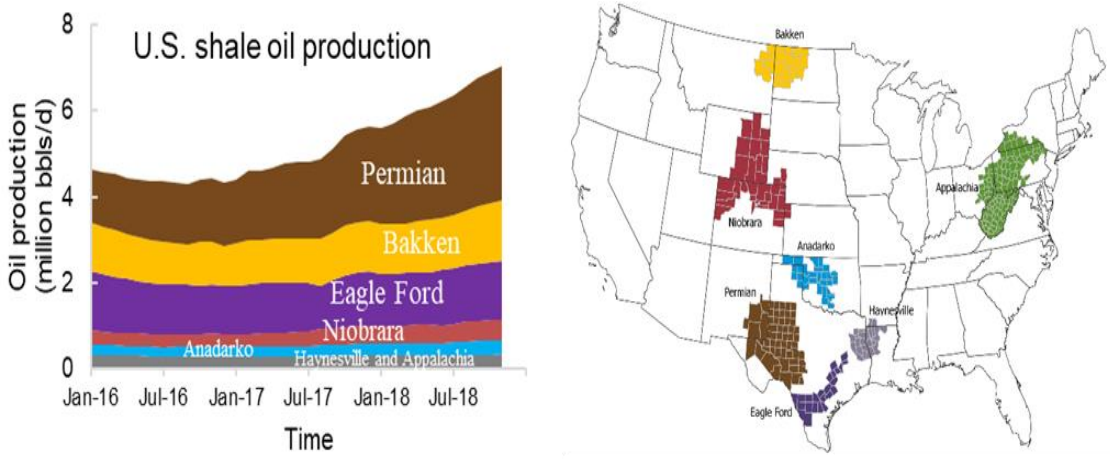


Figure 1. U.S. oil production from major shale plays (Modified from EIA, 2018).

Despite the advancement of the hydraulic-fracturing technologies, oil production from unconventional wells decreases rapidly suffering from lower recovery factors. Enhanced Oil Recovery (EOR) processes are the enabling techniques that would yield more 1.6 to 9 billion barrels of oil with even a 1% incremental recovery (Hawthorne et al., 2013). Miscible gas

injection is the most feasible method to enhance production in shale oil reservoirs (Alfarge et al., 2017; Sheng et al., 2015). Among several gas-injection options, CO_2 injection methods have been evolving in recent years as the most promising methods in terms of technical and profitability aspects. Currently, numerous elements of CO_2 and other solvent injection processes in unconventional resource plays are topics of active research.

In this thesis, a systematic modeling framework was proposed to apply in unconventional shale reservoirs with a focus on the Permian Basin. This approach utilized an integrated workflow that considers geological, geomechanical, multistage fracturing and dynamic reservoir data to model hydraulically fractured wells and simulate CO_2 huff-n-puff enhanced recovery of liquid-rich shale reservoirs.

1.2 Objective

The main objectives of this thesis are the following:

1) Establish an integrated modeling workflow to utilize various subsurface and well data into constructing the robust and holistic multistage hydraulically-well and reservoir model with an aim to predict the primary depletion for unconventional well.

2) Examine CO_2 huff-n-puff process in hydraulically fractured well using both black-oil and compositional reservoir models.

3) Introduce the molecular diffusion concept and study the role of molecular diffusion in realistic reservoir settings under CO_2 huff-n-puff regimes.

4) Evaluate composition variations and its thermophysical properties of multi-components in the near wellbore regions.

1.3 Thesis Organization

Chapter 2 introduces an integrated modeling framework in unconventional reservoirs. The proposed modeling framework allows data integration from geology and geomechanics in constructing the static and earth models. The crucial step relates to constructing multi-stages hydraulic fracturing models to derive complex fracture network where capturing the wide range of hydraulic-fracture treatment and design parameters. Then, fracture network and fracture conductivity were ported into 3D reservoir fluid flow simulator. Additionally, dual-porosity compositional models were utilized to investigate the multi-stages horizontal well performance, diffusion effect, and learn the insights of huff-n-puff CO_2 EOR caused in the near wellbore regions.

Chapter 3 provides the molecular diffusion concept and methodology. The diffusion in both oil and gas phases are introduced where diffusion coefficients have been critically evaluated for further inputs in dynamic compositional reservoir simulation models.

Chapter 4 begins by introducing various simulation scenarios of CO_2 EOR huff-n-puff under comprehensive characterization of static reservoir properties, complex hydraulic fracture network, and a description of natural fractures. Then, simulation results between diffusion and without diffusion are compared after significant cycles of huff-n-puff process. Sensitivity analysis has been investigated under various reservoir quality scenarios and significant levels of diffusion impact.

Chapter 5 presents the simulation results of typical compositions variation around the near well bore regions through different huff-n-puff cycles at the end of the injection, soaking, and production periods. This section also illustrates the evolution of thermophysical properties with the departure in pressure, oil saturation, oil viscosity, and surface tension.

Chapter 6 discusses the limitations and further improvement and finally concludes this research in Chapter 7.

Chapter 2: Integrated Modeling in Unconventional Reservoirs

In this chapter, a thorough framework is proposed to integrate full range of data from geology to geomechanical properties to dynamical reservoir variables and parameters into modeling the enhanced recovery in unconventional resources. The proposed approach consists of three main steps as in the following sections.

2.1 Geological and Mechanical Earth Models

2.1.1 Geological Model

Data from 10 wells (**Figure 2**) in Howard County within the Midland Basin was used to establish a 3D structural model**.** The study area is located in the northwest Midland basin area (**Figure 3**).

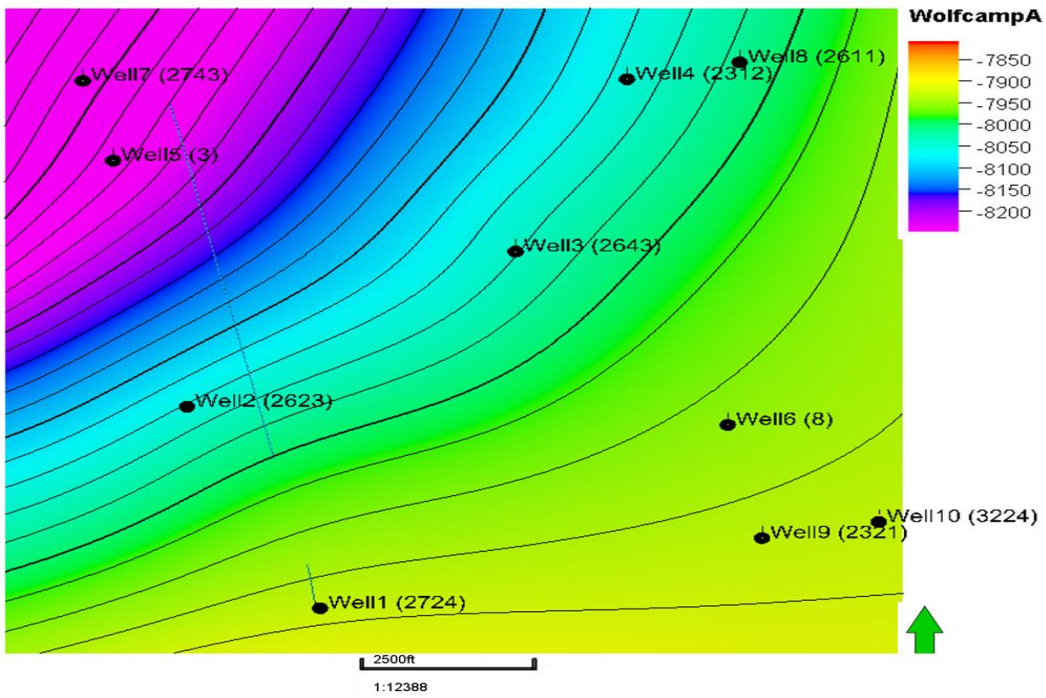


Figure 2. Wolfcamp structure map with well locations of study area.

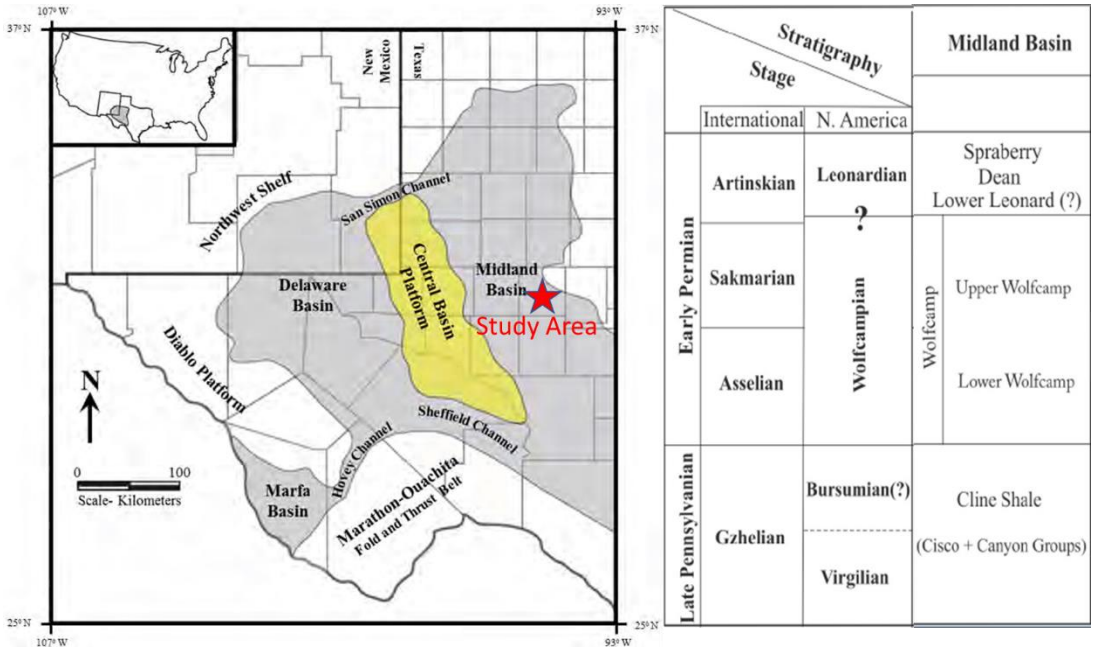


Figure 3. Study Area in the Midland Basin and stratigraphy column (modified from Fu, 2015).

The zone of interest comprises of Wolfcamp formation as the principal target. The upper and lower of Wolfcamp encompass Spraberry, Dean and Cisco, Strawn formations. Formation tops were correlated from well data to set-up the model structure. The 3D grid, size of 1.5 × 2 miles was populated with facies as shown in **Figure 4, 5**.

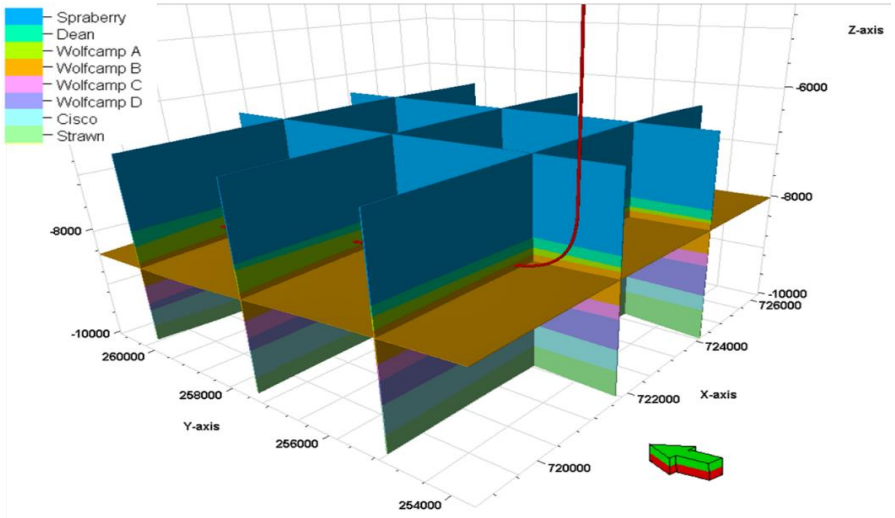


Figure 4. 3D static model encompasses upper and lower of Wolfcamp formations with horizontal well landing in Wolfcamp A.

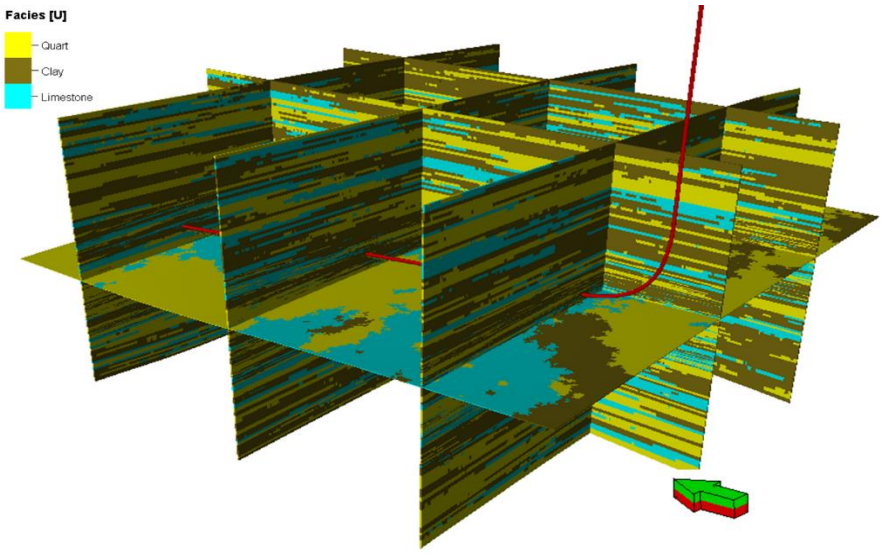


Figure 5. 3D facies model with horizontal well landing in Wolfcamp A formation.

3D facies models were constructed by analyzing well-log properties, such as gamma ray and neutron porosity to be associated with sandstone, carbonate or shale. Figure 6 shows an example of facies log and other available logs used. In this study, Wolfcamp formation was classified into five main rock types based on works reported by Hamlin and Baumgardner (2012) and Kvale et al. (2016). Two of the rock types are classified as sandstone facies, two are mudstone facies and the remaining are carbonates. After characterizing the rock, the facies distribution in 3D structure is populated using sequential indication modeling with constrained upscaled rock types log for all wells. The main parameters and proportion of facies are summarized in **Table 1**. The key Wolfcamp mineralogy includes quartz, carbonate, non-organic shale and organic-rich shale (Blomquist, 2016; Fairhurst et al., 2012; Henry, 2012; Shelokov et al., 2017; Wickard et al., 2016). The contents of these minerals will affect the fracture ability of formation rock and they are related to determination of principal geomechanical properties, such as Young's Modulus, E, and Poisson's ratio, ν.

In this work, the mineral composition distribution model is populated using Sequential Gaussian Simulation (SGS) constrained to both the facies model, and the mineralogical proportions from core studies in the area of interest by Gupta et al. (2017). Standard mineralogical components of rock types in Wolfcamp formation include quart, carbonate, and clay mineral contents. 3D mineral composition distribution models are generated for each of these components.

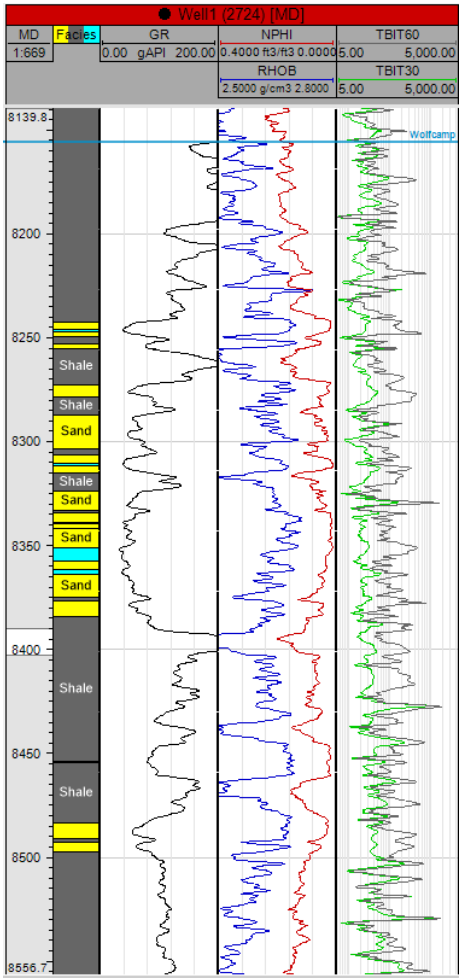


Figure 6. Facies log and available logs

The key petrophysical properties such as porosity and permeability were then spatially populated. We constructed 3D porosity model using Sequential Gaussian Simulation (SGS) constrained to previously built facies model and honoring available upscaled well logs in the

study area. For permeability model, we employed SGS with collocated kriging with constrained porosity model. The resultant models show in **Figure 7, 8** indicating the matrix porosity in the range of 4 to 12 % and matrix permeability of 0.01 to 10 μD.

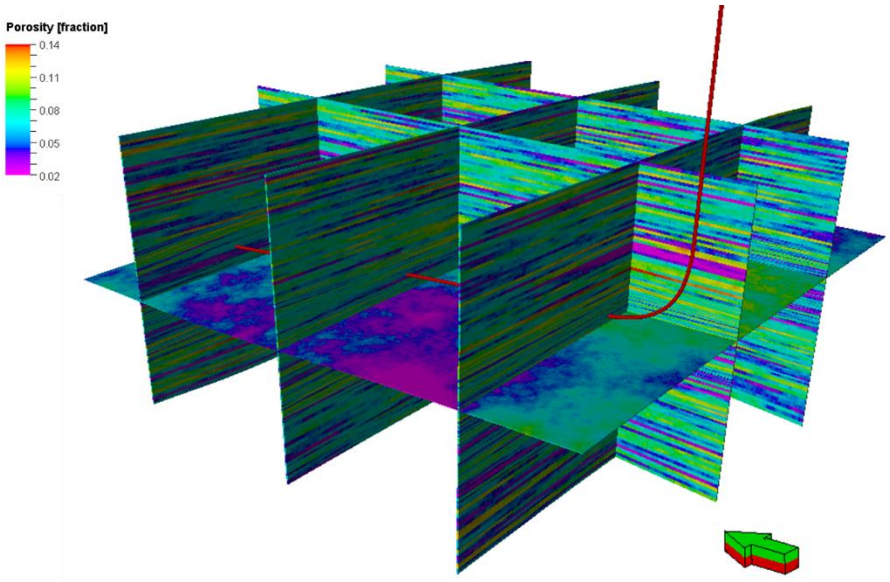


Figure 7. 3D porosity model with horizontal well landing in Wolfcamp A formation.

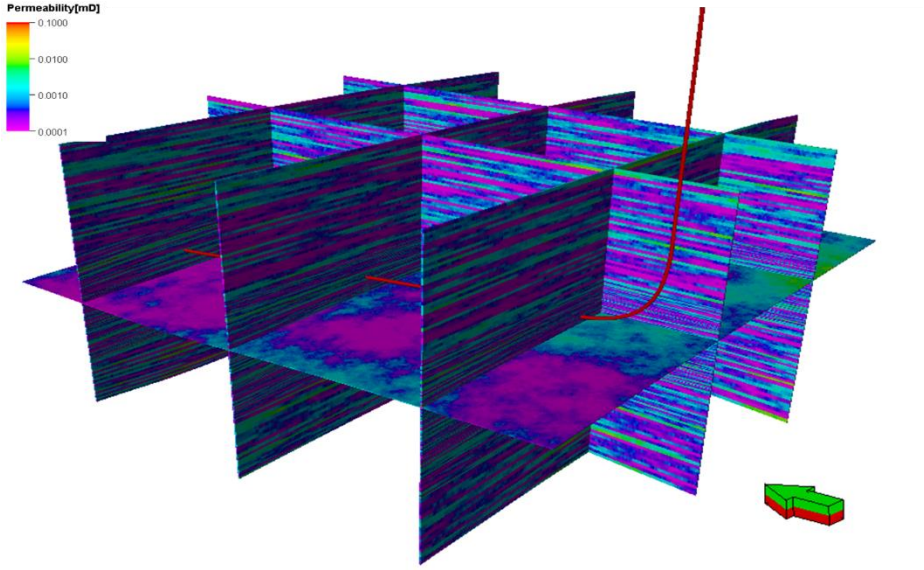


Figure 8. 3D permeability model with horizontal well landing in Wolfcamp A formation.

Table 1. Minimum and maximum values of the major petrophysical, mineralogical and variogram inputs employed in Design of Experiment (DoE).

Parameters	Min	Max
Quartz, %	16	41
Carbonate, %	3	56
Clay, %	10	56
Matrix porosity, %	4	12
Matrix permeability, μD	0.01	10
Major anisotropy range of variogram, ft	1,000	5,000
Minor anisotropy range of variogram, ft	100	500
Vertical anisotropy range of variogram, ft	4	10

2.1.1 Mechanical Earth Model

To construct 3D mechanical earth models including Young's Modulus and Poisson's Ratio, **Eq.1** and **Eq.2** (Miskimins et al., 2002; Zoback, 2007) were used where typical inputs are from available sonic well log data. **Figure 9** exhibits the main processed well-log curves of Well 03. The first three tracks in the left comprise of caliper (CALI), gamma ray (GR), spectral gamma ray (uranium, thorium and potassium) and bulk density (RHOB). Facies column in the middle shows three main lithologies in shale, carbonate and sand which have been shaded in brown, light blue, and yellow respectively. In addition, the velocity of compressional waves (V_p), and velocity of shear waves (V_s) are shown in the next track. These two key parameters are used to determine E and ν using Eq.1 and Eq. 2.

$$\nu = \frac{V_p^2 - 2V_s^2}{2\left(V_p^2 - V_s^2\right)} \quad (1)$$

$$E = \frac{\rho(3V_p^2 - 4V_s^2)}{2\left(V_p^2 - V_s^2\right)} \quad (2)$$

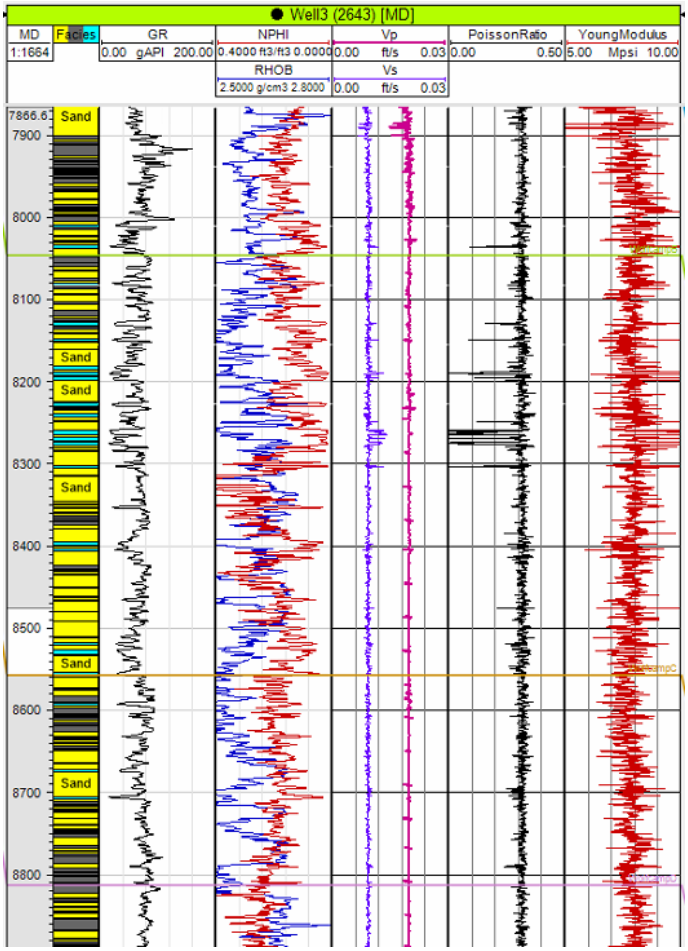


Figure 9. Principal geomechanical properties derived from sonic and other logs (last 3 tracks on the right side).

Available sonic well-log only provides V_p data where the counterpart V_s was not recorded. Quality sonic data is rarely measured in most vertical wells resulting in high uncertainty in determination of geomechanical properties. To alleviate that uncertainty and compensate for the lack of well information, this study utilizes published lithological data in Wolfcamp and empirical relationships to derive V_s. Core data from different studies showed the minerology in Wolfcamp as quartz ranging from 16% to 41%, carbonates from 3% to 56% and clay minerals from 10% to 56% (Approach Resources, 2010; Gupta et al., 2017). Empirical relationship between mineral contents and geomechanical properties was imparted via V_p, V_s.

(Castagna et al., 1984) found the distinct difference in V_p/V_s for limestones, dolomites and clean sandstones (Figure 10).

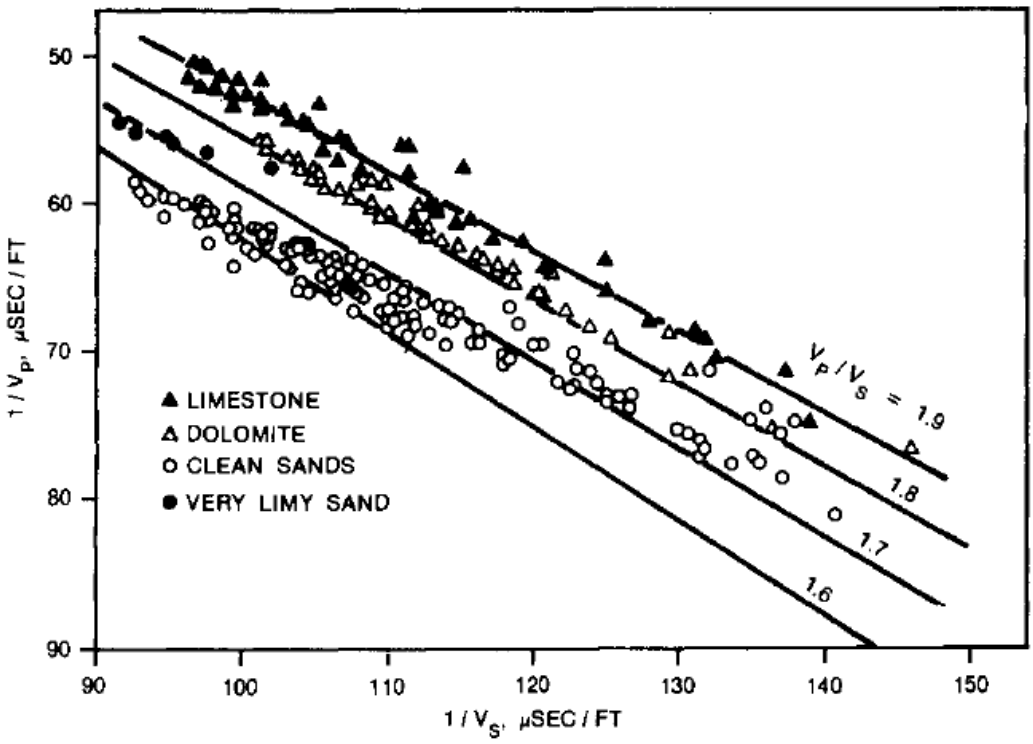


Figure 10. Strong correlation between V_p and V_s with distinct separation among limestone, dolomite and clean sandstone (from Castagna et al., 2014).

In addition, V_p/V_s ratio is higher in clay-rich rock (Castagna et al., 1984) than in quartz and carbonate-rich rock (**Figure 10**). The estimated V_s was populated using above empirical relationship. Hence, the two tracks on the rightmost in **Figure 9** shows the estimated E and ν which will be used to spatially populate the 3D mechanical earth models (**Figure 11**). V_p and V_s from two available wells were upscaled. Anisotropy range of 500 ft in the horizontal direction and 10 ft in the vertical direction were set to fit the variogram model with upscaled data points. Then, sequential gaussian simulation was used to generate 3D models of V_p and V_s using variogram parameters from the upscaled model with constrained by the previous facies model

and honoring available well logs. It is challenging to identify intrinsic factors affecting anisotropy in V_p, V_s. Sources of such anisotropy can be many including variations in rock/mineral texture, rock fabric, pore architecture (fractures, fissures, …), meso-scale intercalations of the formations and sub-formations, and rock-fluid interactions amongst others. In this study, I have not critically and directly examined the level of V_p, V_s anisotropy.

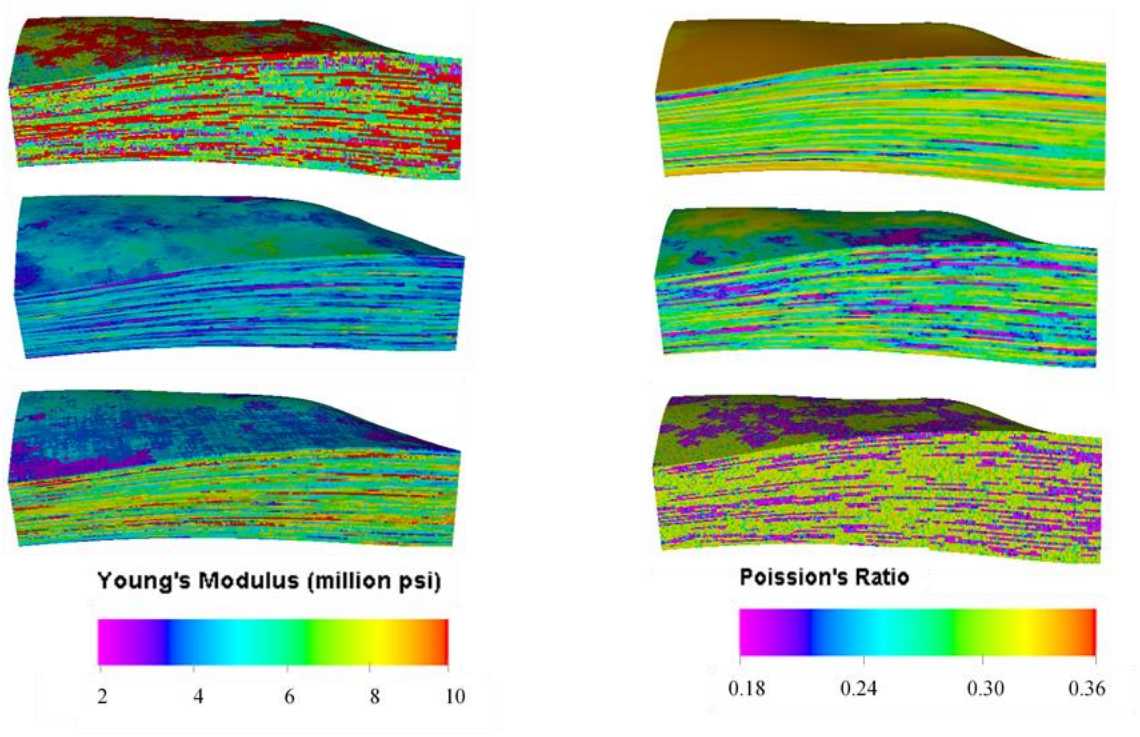


Figure 11. 3D Young's Modulus and Poisson's Ratio from various realizations of mineralogical and geological inputs.

2.2 Hydraulic-Fracture Modeling

Fractures hydraulically created are not only depend on the elastic properties of reservoir rocks, but also fracturing treatment and design process. Therefore, incorporating parameters related to hydraulic-fracture treatment design is necessary for evaluating its impact on production performance, or further injection management strategy such as CO_2 huff-n-puff process. The

hydraulic-fracture modeling workflow involves extracting geological and geomechanical properties from previously discussed static models and incorporating them with multi-stages fracture design and pumping schedule data in a fracture simulator using GOHFER (Baree and Associates 2017).

2.2.1. Main Hydraulic Fracturing Model Inputs

The hydraulic-fracture treatment and design parameters comprise several fracture stages, number of stages, cluster spacing, proppant type and concentration, and fracture-fluid type and volume. These inputs play vital roles in the 3D hydraulic-fracture model to create complex fracture geometry and network. The numbers for these inputs are considered by various operators in Midland basin with different applied completion techniques such as plug-and-perf and sliding-sleeves. In Wolfcamp formation, the lateral lengths drilled from 4,000 ft to greater than 13,000 ft (Alimahomed et al., 2017; Blomquist, 2016) to maximize the completion efficiency. In my thesis, a range of normalized lateral of 2,000 ft is examined to allow sufficient run time with available computational resources. Thus, number of stages, cluster spacing, and cluster density are reasonably determined in **Table 2**. These key parameters can be found in previous studies (Alimahomed et al., 2017; Beard, 2011; Encana, 2015).

Table 2. **Hydraulic-fracturing design parameters used in this study.**

Parameter	Value
Lateral length, ft	2,000
Number of stages	10
Cluster spacing, ft	20
Number of clusters per stage	6
Slurry rate, bpm	75
Fluid type	Slick water
Fluid volume, gal/ ft	2,000

Proppant type	Sand 40/70
Proppant concentration, lb/ gal	1-3

2.2.2. Pumping Schedule and Design

To model the realistic hydraulic-fracturing job, this thesis implemented a multi-stage "plug and perf" process, which is the most common completion techniques to stimulate the horizontal unconventional wells used by many operators in the Midland Basin. The "plug and perf" involves some mechanical isolations by setting of bridge plugs in stages, followed by perforating and fracturing of formation in the well for each stage. Generally, the first fracture stage is performed near the toe of the horizontal well. The process is repeated in the subsequent stages until reaching the heal area of the well or at a designed interval. In GOHFER, it can be done by defining specific perforation intervals associated to ball dropping events. This allows only specified completion stage opened for proppant and fluid penetration during the pumping process. **Figure 12** mimics the real plug and perf pumping schedule for 10 stages of a fracturing job starting from the toe of the horizontal wellbore. Each stage starts with an initial phase where treating fluid is pumped at 75 barrels per minutes (bpm) carrying 1 pound per gallon (lbm/gal) proppant sand 40/70, and proppant concentration increases gradually to 3 lbm/gal at the end of the first phase. Then, flushing fluid is pumped with no proppant in the second phase, and the plug off is set in the final phase to assure the proppant holds fractures open after the main hydraulic fracture treatment period.

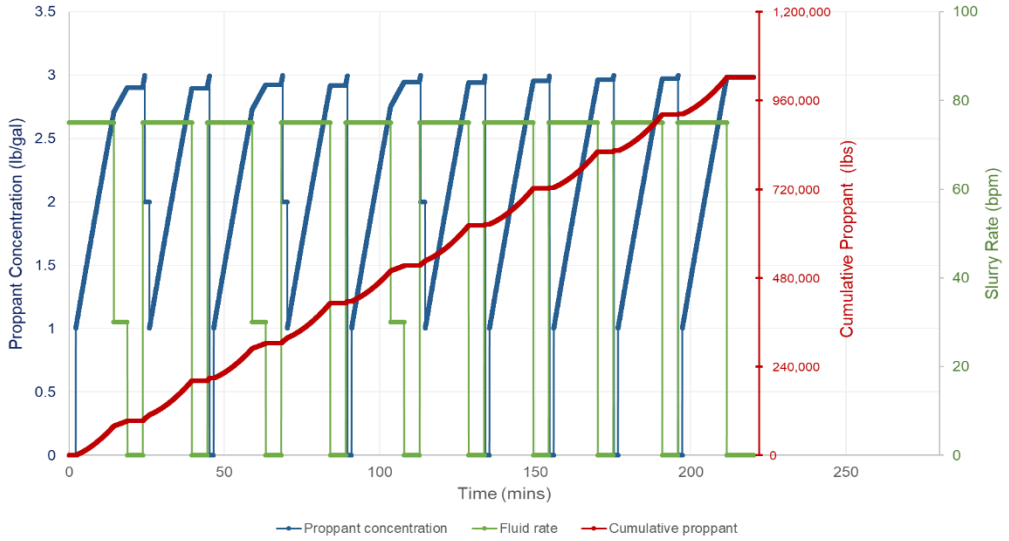


Figure 12. Plug-and-perf hydraulic-fracturing schedule used in this study.

2.2.3. Modeling Hydraulic-Fracture Geometries and Network

To capture the whole range of uncertain parameters, an experiment and design method, Plackett-Burman was implemented to generate 120 scenarios of hydraulic fracturing design. The combination of the above geological and geomechanical models along with the multi-stage fracturing process results in a bi-wing series of parallel fracture. **Figure 13** depicts the fracture network over multiple fracture clusters and stages created using GOHFER for the base-case reservoir model. Also, **Table 3** presents summaries the statistical description of the fracture geometries and important fracture properties derived from simulated fracture models. Single hydraulic fracture half-length (X_f) typically lies in the range of 100 ft to approximately 800 ft, but some induced fractures extend up to 1,000 ft from lateral due to the asymmetric growth and propagation during the treatment process. On the other hand, hydraulic-fracture width is most likely to vary between 0.03 to 0.3 inch and mainly driven by proppant sizes and volumes. Also,

fracture conductivity ($k_f w_f$) is another key driver for stimulation performance. Our sensitivity analysis shows that $k_f w_f$ ranges from 1 md-ft up to more than 130 md-ft.

Table 3. Simulated hydraulic-fracture network for the base case model.

Parameter	Min	Max	Mean
Fracture half-length, ft	100	770	640
Fracture width, in	0.036	0.258	0.09
Fracture height, ft	20	195	157
Net Pressure, psia	0	1360	790
Cluster hydraulic surface area, ft^2	131,700	162,400	148,025
Stage hydraulic surface area, ft^2	564,400	635,000	592,100
Effective Conductivity, md*ft	1.2	134	30

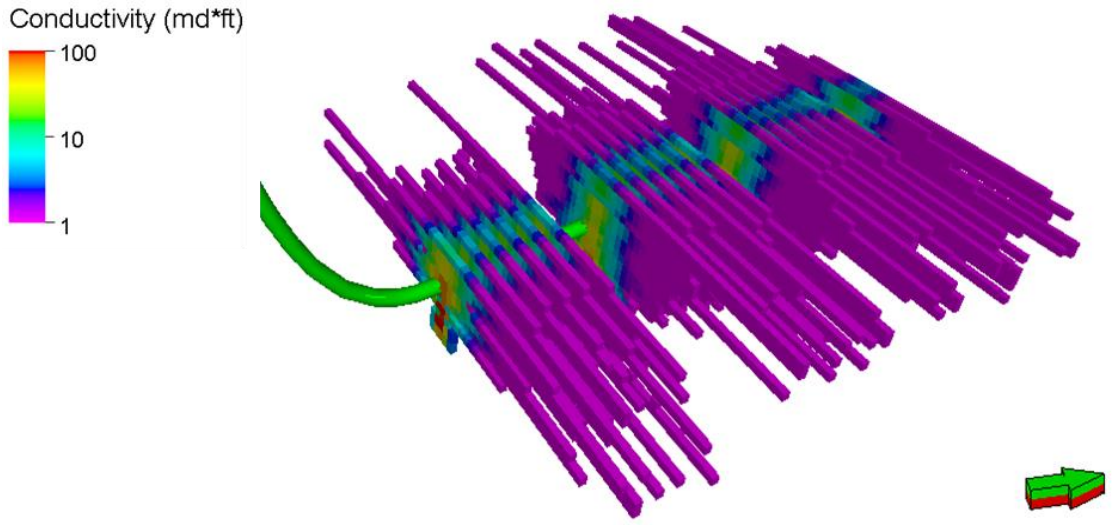


Figure 13. Example of resulting multi-stage hydraulic-fracture network from the base-case reservoir model.

Subsequently, the grid of the simulated hydraulic-fracture geometry and conductivity are ported into a 3D reservoir fluid flow simulator to simulate and investigate primary and enhanced recovery processes for the stimulated horizontal well in unconventional reservoirs.

2.3 Reservoir Settings and Dynamic Model

2.3.1 Static Model

Table 4 summaries the key model settings and reservoir parameters from the base-case reservoir model. This table states only the average values of the heterogeneous distributions of porosity and permeability. The gravity-capillary equilibrium for the initial fluid distribution was assumed for simplicity in modeling.

Table 4. Basic reservoir settings for the base-case reservoir model.

Parameter	Average value
Reservoir depth, ft	8,000
Reservoir temperature, °F	165
Initial reservoir pressure, psi	4,000
Average matrix permeability, mD	0.0013
Average matrix porosity, %	7
Initial water saturation	0.35
Initial oil viscosity, cp	2
Grid size, ft	20 × 20 × 5
Total number of blocks	3,958,720

2.3.2 Compositional Fluids and Rock Physics

For the dynamic in simulation, this thesis used plausible reservoir in-situ in both black-oil and composition of a liquid-rich from unconventional reservoirs reported by Whitson and Sunjerga, 2012. The oil has a gravity of 37.7 API (STO), a solution gas-oil ratio of 500 scf/STB and a bubble-point pressure of 2260 psi at 165 ^{o}F. For primary depletion purposes, both black-oil and compositional models are investigated to predict the well performance. Then, only compositional model will be used for further enhanced recovery modeling under CO_2 huff-n-puff process. It is clear that black-oil model is not sufficient for expected CO_2 miscible occurred in the reservoir once the huff-n-puff process is implemented. Furthermore, molecular diffusion requires compositional flow to model accurately. In addition, to manage the simulation run-time

to a reasonable level, a 27-component compositional-fluid model was lumped into five pseudo-components that capture the main properties of the fluid and simplify the compositional simulation. The authors explored three lumping techniques such as lumping by mixing, mole fraction and molecular weight to compare with the full-component phase envelope (**Figure 14**). **Table 5** presents the mole percentages of five pseudo-components from the most appropriate technique mimicking the original phase behavior.

Table 5. Lumped composition for in-situ liquid-rich oil unconventional reservoir.

Component	Liquid mole	Vapor mole	Total
CO_2	1.39	2.32	1.39
C_1	34.88	90.17	34.88
$C_2 - C_4$	8.52	6.69	8.52
$C_5 - C_7$	5.87	0.7	5.87
C_{7+}	49.34	0.07	49.33
Total	100	100	100

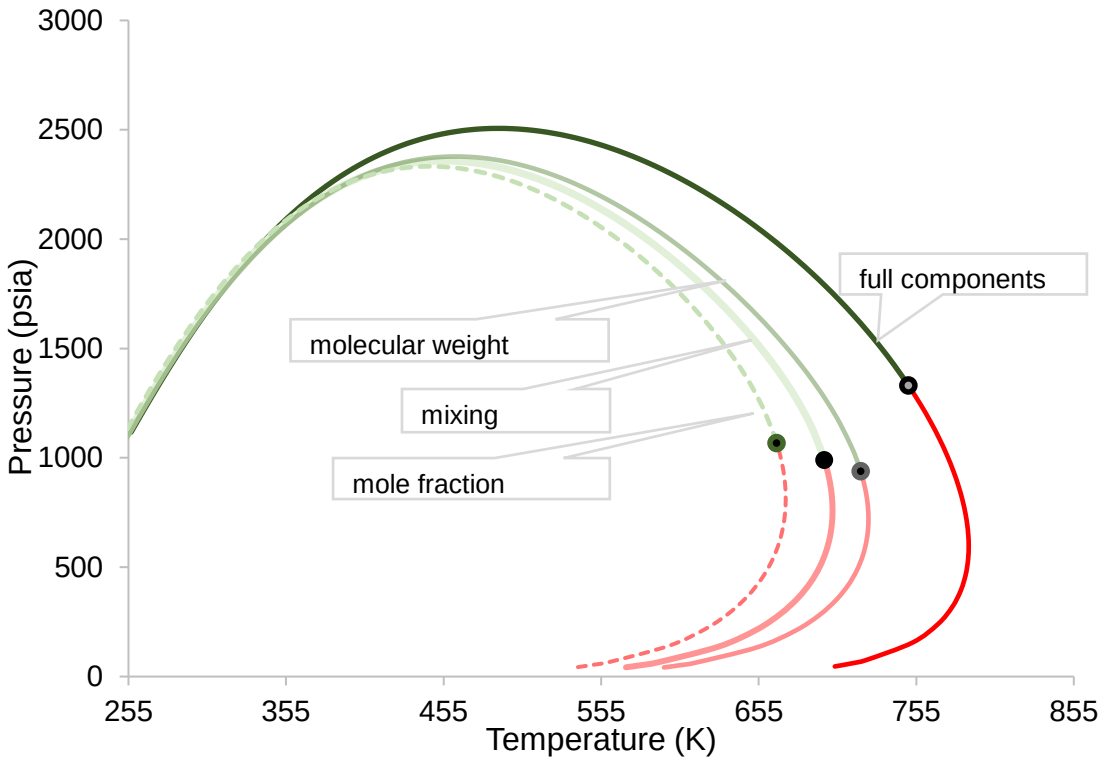
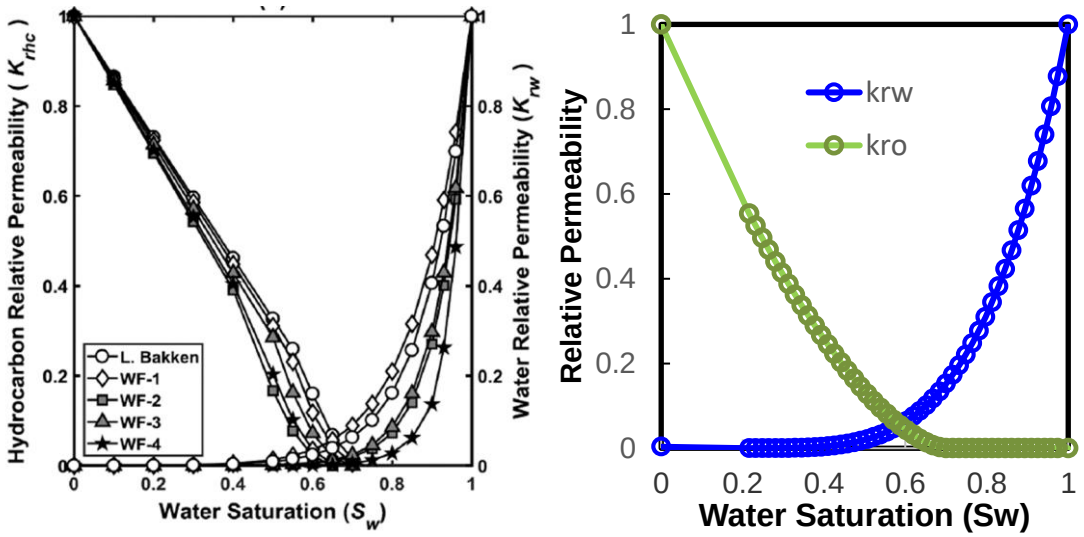


Figure 14. Compositional lumping by different PVT techniques

In term of rock physics, this research report employed two relative permeability systems, one for shales and the latter for natural fractures. For shale relative permeability curves, critical saturation points and Corey exponent numbers were entered to relatively match the generated curves (**Figure 15b**) with typical shale samples of Wolfcamp 1 (WF-1) from Ojha et al. (2017) (**Figure 15a**). Relative permeability curves for natural fractures were simply customized following linear Corey's correlation. Input parameters such as critical saturation points, residual saturation points, and Corey exponent numbers are summarized in **Table 6**.



(a) **(b)**

Figure 15. Relative permeability curves for typical shales formation (from Ojha et al., 2017) in (a) and generated relative permeability curves used in this study in (b).

Table 6. Inputs for rock physics model used in shale system.

Parameters	Shale system	Natural-fracture system
Residual Oil Saturation S_{orw}	0.3	0.3
Critical Water Saturation S_{wcrit}	0.2	0.2
Critical Gas Saturation, S_{gcrit}	0.06	0.06
End point k_{rocw} at Connate Water	1	1
End point k_{rwiro} at Irreducible Oil	1	1
End point k_{rogcf} at Connate Gas	0.8	0.8
Corey exponent for oil	1.6	1

Corey exponent for water	4	1
Corey exponent for gas	3	1

2.3.3 Well Model

Single horizontal well with multi-stages hydraulic fractures was considered for CO_2 EOR huff-n-puff modeling and evaluation. Perforation was added for the entire 2,000 ft of lateral length. Well data and configuration used in hydraulic fracturing treatment and design step were consistently carried over to reservoir modeling step. Hence, injection process during hydraulic fracturing at well level should not been repeated. Instead, well was begun to model for initial production and further EOR purpose.

2.3.4 Reservoir-Model Settings

Heterogeneous 3D reservoir model size of approximately 3.96 million of grid cells (178 × 278 × 80 grids) is developed with dual-porosity functionality. The lateral grid size in this model is 20 ft × 20 ft in the X and Y directions, and the vertical cell thickness is on average 5 ft within the main landing zone, Wolfcamp A, and coarser in the upper Dean and lower Wolfcamp B formations. Discrete Fracture Network (DFN) was built as a part of the integrated study to characterize the natural fractures existing in the area. Data for fracture intensity, fracture aperture and height from a comprehensive review by (Gale et al., 2015) were used to generate a complex DFN model in this step. Additionally, porting of the hydraulic-fracture geometry onto a reservoir simulator is not a trivial task. In this work, the underlying presumption was that non-trivial conductivity obtained from the fracture simulation is purely due to induced fracturing. With this assumption, the property array of effective fracture-conductivity is mapped onto a property array of transmissibility multipliers using normalized effective conductivity. Grid cells with transmissibility multiplier equal to 1 represent non-stimulated cells, while those with larger

values indicate the simulated cells with higher effective conductivity. Using transmissibility multipliers, in this manner, is analogous to effective permeability enhancement due to the hydraulic fractures. This enables the reservoir simulator to capture the effect of complex fracture network.

Discussion in this thesis covers a thorough inspection of the fluid-transport process and the changes in compositions and thermophysical properties in the matrix within the stimulated reservoir volumes (SRV). Four distinct regions are defined around the hydraulically fractured horizontal well using total mole-fraction of CO_2 contacted by the rock matrix after the first injection cycle. The innermost region adjacent to the wellbore wall, Region 1 (**Figure 16**), is defined with greater than 0.5 of CO_2 mole fraction. Accordingly, Regions 2, 3, and 4, are stated with maximum values of CO_2 mole fraction of 0.25, 0.1 and 0.01, respectively. In terms of volume proportions, Regions 1, 2, 3 and 4 account for 8%, 17%, 35%, and 40% of total SRV, respectively. A part of subsequent sections in this thesis evaluates the variation of compositions and thermophysical properties in these four distinct regions.

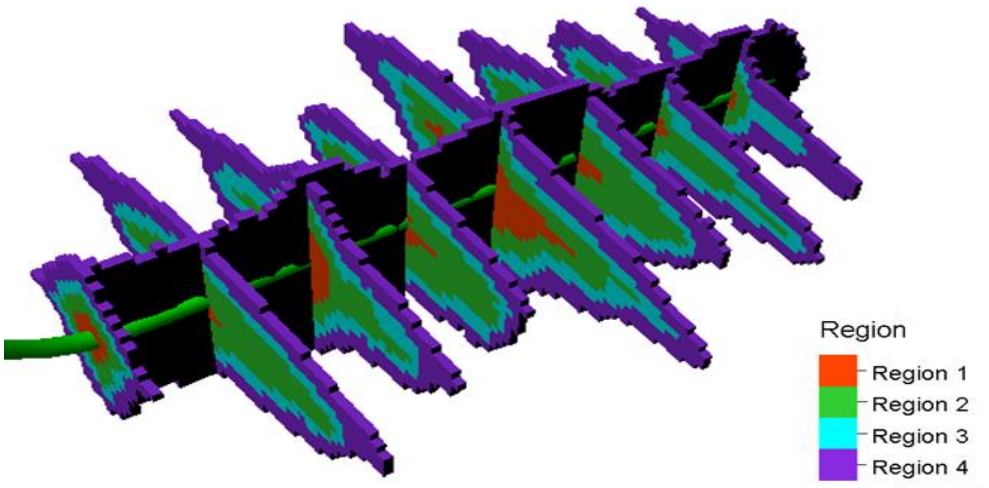


Figure 16. Definition of 4 distinct reservoir partitions of the stimulated regions surrounding hydraulically fractured well.

2.3.5 Huff-n-Puff Processes

To model the huff-n-puff CO_2 EOR process in unconventional reservoirs, I used the calibrated multistage hydraulically fractured horizontal well completed in the Wolfcamp shale formation as specifically described in the previous section in this thesis. One complete huff-n-puff CO_2 cycle consists of 1-month injection, 1-month soaking, and 3-month production periods. As shown in **Figure 17**, only six years of this process is modeled resulting in 14 cycles in total to ensure a reasonable simulation time.

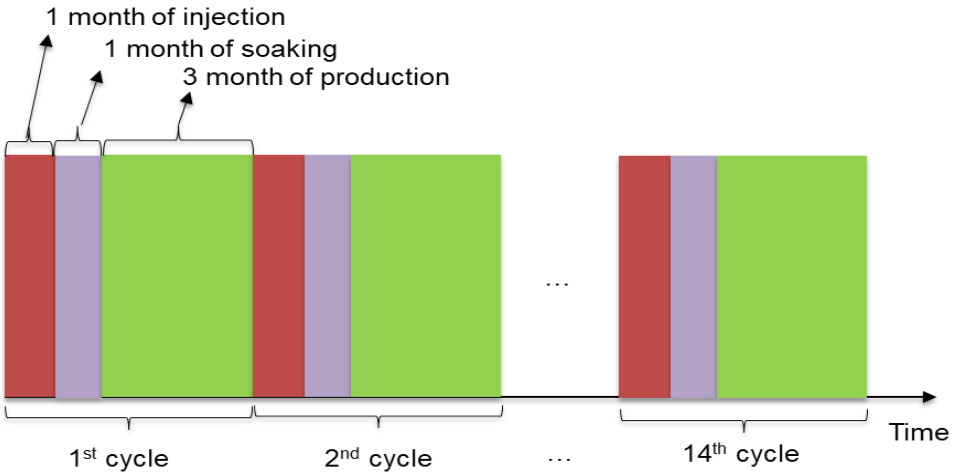


Figure 17. Well scheduling of CO_2 cyclic injection process.

Chapter 3: Molecular Diffusion Models

For ultra-low permeability reservoirs like unconventional shale in Wolfcamp, molecular diffusion becomes a crucial mechanism for transport and mixing of CO_2, oil and gas. Numerical simulation approach proposed in this thesis allows diffusive flow for multiple components in oil and gas phases. Theoretically, Fick's laws of diffusions (Eq. 3) describes the diffusion flux from high concentration regions to low concentration regions.

$$J_i = -cD_i \frac{\partial x_i}{\partial d} \tag{3}$$

Where J_i is the molar diffusion flux of component i and c is the total molar concentration given by $c = 1/v_m$, where v_m is the molar volume of the mixture. In addition, D_i is the diffusion coefficient of component i, and $\frac{\partial}{\partial d}$ the gradient in the direction of flow.

Further study in this thesis involves in CO_2 diffusion and variation in composition in tight rock matrix condition at different stages of the CO_2 huff-n-puff process. Hence, **Figure 18** presents the suggested workflow to estimate the diffusion coefficients in both liquid and gas hydrocarbons. The diffusion coefficients table result from this workflow will be used as the inputs for diffusion model in dynamic compositional reservoir simulation.

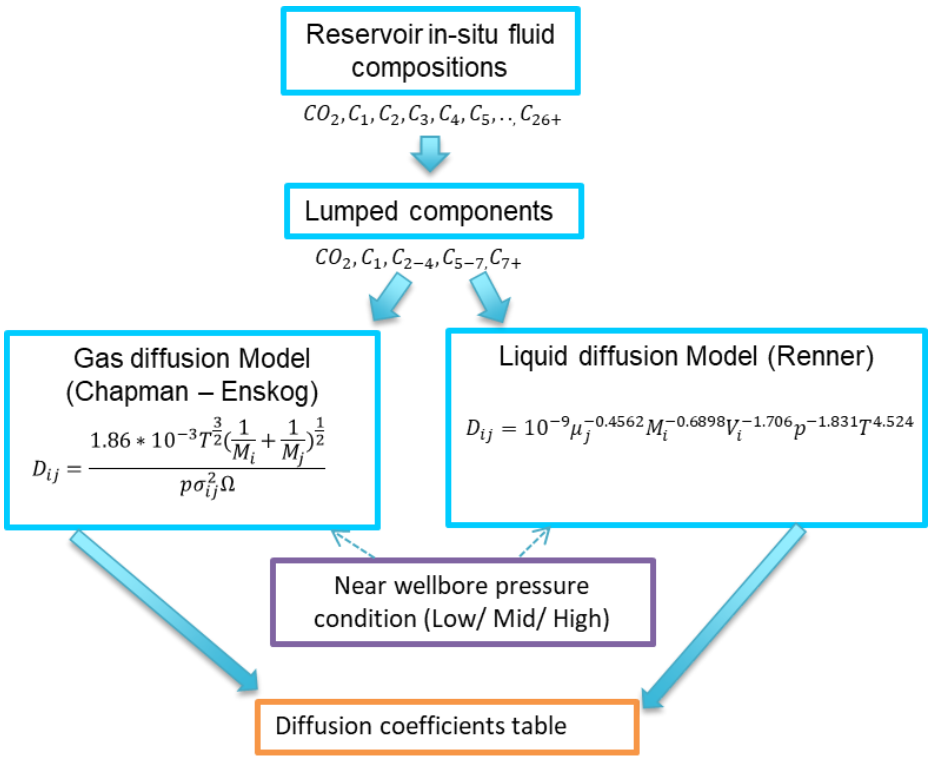


Figure 18. Proposed workflow of diffusion coefficients method used in this study.

3.1 Liquid-Phase Diffusion

Diffusion coefficients in liquid hydrocarbons of the lighter lumped components including CO_2, methane, and ethane to butane are calculated using the correlation developed by Renner (1988). This empirical equation (**Eq. 4**) considers diffusion as a function of the liquid viscosity, molecular weight of gas, molecular volume of gas, pressure and temperature.

$$D_{ij} = 10^{-9} \mu_j^{-0.4562} M_i^{-0.6898} V_i^{-1.706} p^{-1.831} T^{4.524} \quad (4)$$

Where D_{ij} is the diffusion coefficient in m^2/s, μ_j is the liquid viscosity in cp, M_i is the molecular weight of the gas in g/g mol, V_i is the molecular volume of the gas in cm^3/g mol , p is the pressure in psia, and T is the temperature in degrees Kelvin.

3.2 Gas-Phase Diffusion

To determine the gas diffusion coefficients, the recommended method developed by Hirschfelder et al. (1949) based on Chapman-Enskog theory. **Eq. 5** shows the expression for binary diffusion coefficients in cm^2/s. For each lumped component, the binary coefficients with other species present were calculated, and generated an average diffusion coefficient for the component in the fluid studied.

$$D_{ij} = \frac{0.00186T^{\frac{3}{2}}}{p\sigma_{ij}^2\Omega}\left(\frac{1}{M_i}+\frac{1}{M_j}\right)^{\frac{1}{2}} \tag{5}$$

Where T is the absolute temperature in Kelvin, p is the pressure in atmospheres, $M_i$and M_j are the molecular weights, and σ_{ij} is the collision diameter in angstroms. Ω is the collision integral of the Lennard-Jones potential, obtained from tabulated values as a function of the interaction energy between the components. **Table 7** shows the parameters used to calculate Ω for the components present in our simulation fluid.

Table 7. Lennard-Jones potential parameters for the components.

Component	σ_{ij} (A)	ε_{12}/k_B (°K)
CO_2	3.941	195.2
CH_4	3.758	148.6
C_2H_6	4.443	215.7
C_3H_8	5.118	237.1
nC_4H_{10}	4.687	531.4
iC_4H_{10}	5.278	330.1
nC_5H_{12}	5.784	341.1
nC_6H_{14}	5.949	399.3

3.3 Pressure and Temperature Sensitivity to Diffusion Coefficients

This section discusses the diffusion process while considering pressure change during the huff-n-puff operations depending on its cycle of injection, soaking or production. Using the

proposed diffusion models, **Figure 19** presents the estimated diffusion coefficients where CO_2 and individual components diffuse in gas and liquid hydrocarbon respectively at various pressure and temperature conditions. In general, lighter components such as C_1, CO_2, C_2 yield larger diffusion coefficients in both gas and oil system. Also, diffusion coefficients tend to increase parabolically as a result of decrease in pressure where these numbers decrease with the decrease in temperature. Assuming isothermal reservoir condition during the depletion and huff-n-puff process, only diffusion coefficients change with various pressure regimes were investigated in the dynamic reservoir models.

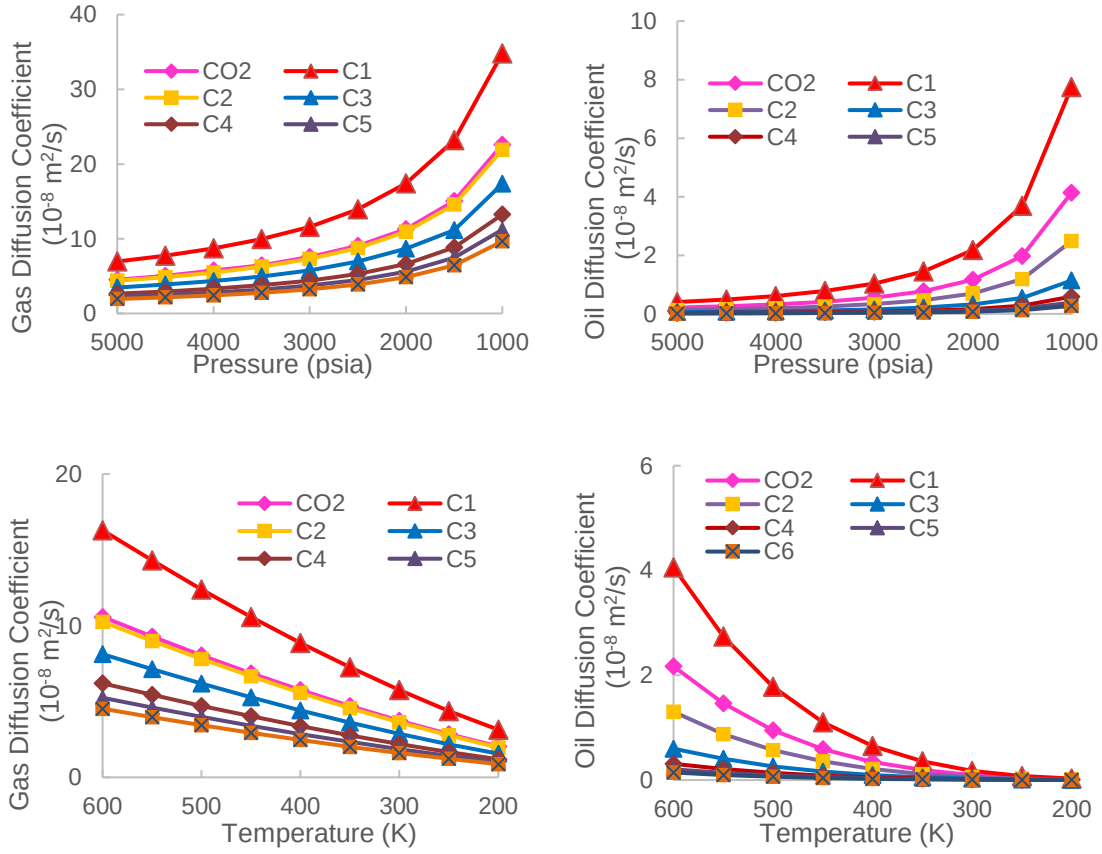


Figure 19. Diffusion coefficients variation with pressure and temperature.

3.4 Lumped-Component Diffusion Coefficients

Diffusion coefficients for lumped components in both gas and liquid hydrocarbon are then generated using molecular-weight averaged method as shown in **Eq. 6** below, where D_j is the diffusion coefficient of lumped components in m^2/s, D_i in m^2/s and M_i are diffusion coefficients and molecular weights of single components respectively associating to the lumped components.

$$D_j = \frac{\sum M_i D_i}{\sum M_i} \tag{6}$$

Ultimately, **Table 8** and **Table 9** summarize the estimation of diffusion coefficients in liquid phase and gas phase at three different pressure scenarios, i.e. 4,900 psia, 4,000 psia and 3,000 psia and fixed temperature at 345^{o}K. In gas diffusion, the collision parameter σ is ignored for C_{7+}, so diffusion for C_{7+} in the gas phase is not considered in this study. In any cases, heavy-end components will have insignificant molecular diffusion in the vapor phase. This study uses these three sets of diffusion coefficients to model the molecular diffusion under multiple cycles CO_2 huff-n-puff process in liquid-rich unconventional reservoirs. In addition, numerical modeling and sensitivity analysis will be performed to investigate the compositional variation using different sets of diffusion coefficients.

Table 8. Liquid-phase diffusion coefficients at three different pressures.

Lumped component	D (E^{-8} m^2/s) at P = 4900 psia	D (E^{-8} m^2/s) at P = 4000 psia	D (E^{-8} m^2/s) at P = 3000 psia
CO_2	2.5	3.7	6.2
C1	3.4	5.0	8.5
C2-C4	0.31	0.46	0.77
C5-C7	0.034	0.05	0.085
C7+	0.0033	0.0049	0.0083

Table 9. Gas-phase diffusion coefficients at different pressures.

Lumped component	D (E^{-8} m^2/s) at P = 4900 psia	D (E^{-8} m^2/s) at P = 4000 psia	D (E^{-8} m^2/s) at P = 3000 psia
CO_2	7.4	9.1	12.1
C1	7.2	8.9	11.8
C2-C4	5.7	8.2	10.9
C5-C7	3.1	6.3	8.4
C7+	-	-	-

Chapter 4: CO_2 Huff-n-Puff Reservoir Simulation

This chapter introduces various scenarios of CO_2 huff-n-puff reservoir simulation models which comprehend detailed characterization of the static reservoir properties, complex hydraulic fracture network, and a description of natural fractures. ECLIPSE compositional simulator has been used with dual-porosity mode to enable the fluid flow both in matrix and natural fracture systems. In addition, the diffusion physics for both gas and liquid phases are included to enable the molecular diffusion mechanism in very tight rock matrix environment. Different scenarios of reservoir quality and various significant levels of diffusion effect will be also investigated to the oil enhancement. As mentioned in **Table 8** and **Table 9**, three different operating pressures were involved to calculate different diffusion coefficients for specific components in both oil and gas phases. High pressure condition yields low diffusion coefficients, namely "low" in the following simulation description in **Table 10**. Accordingly, low pressure, i.e. 3000 psia will turn out the numbers at "high" cases. Several assumptions have been made in the simulation models:

- Regional 3D geological and earth models were constructed based on limited available well data
- Empirical correlations used to compute Young Modulus and Poisson's ratio
- Impact of natural fracture to hydraulic fracture propagation was negligible
- Fix huff-n-puff design for injection rate, cycle length was assumed to be constant through cycles

Eventually, 12 simulation cases as described in Table 10 have been completely run and analyzed which capture the uncertainty of reservoir quality, and diffusion coefficients effect due to the change in reservoir pressure and temperature at different stages of the huff-n-puff process.

Table 10. Simulation cases description.

Cases	Reservoir Model	Mean matrix porosity (%)	Mean matrix permeability (10^{-3}mD)	Diffusion Model	Fracture Model
Case 1 – Base case without diffusion	Moderate	7	1	No	✓
Case 2 – Base case with diffusion	Moderate	7	1	Mid	✓
Case 3	Moderate	7	1	Low	✓
Case 4	Moderate	7	1	High	✓
Case 5	Low	5	0.1	No	✓
Case 6	Low	5	0.1	Mid	✓
Case 7	Low	5	0.1	Low	✓
Case 8	Low	5	0.1	High	✓
Case 9	High	9	10	No	✓
Case 10	High	9	10	Mid	✓
Case 11	High	9	10	Low	✓
Case 12	High	9	10	High	✓

4.1 CO_2 Huff-n-Puff Diffusion Incremental Recovery

This section compares the modeling results between Case 1 (base reservoir-quality, no diffusion) and Case 2 (base reservoir-quality, diffusion). **Figure 20** presents the production performance of these two cases. It can be obviously seen that in the first 500 days with 4 cycles of huff-n-puff, production response from diffusion effect is ambiguous. Incremental oil recovery in diffusion is insignificant of 1% compares to without diffusion. It can be explained that diffusion process occurs at a very slow pace and CO_2 component faces extremely difficult in contacting with hydrocarbon components in the matrix. Therefore, in the first few cycles of huff-n-puff, most oil produced comes from natural fracture media and hydraulic fracturing channel.

Once more cycles are followed, CO_2 is more diffused into the rock matrix thanks to diffusive flux from high concentration areas near the well bore to low concentration areas farther away. Then, CO_2 tends to swell and push the hydrocarbon components out of the rock matrix. Subsequently, after approximately 2,200 days with 14 cycles of huff-n-puff, significant

incremental oil recovery of 6% is remarked due to diffusion effect. A significant reduction in the Gas Oil Ratio (GOR) occurred in diffusion which is a consequence of the molecular diffusion process as the CO_2 component diffuses into the matrix freely. Unlike the diffusion, CO_2 tends to flow back in the well once it is brought back on production because most of injected CO_2 retain in the fracture system without diffusion inputs. Figure 21 illustrates the CO_2 total mole fraction in the near wellbore area with and without diffusion at the end of soaking period. It is clearly observed that diffusion allows more CO_2 to spread over the larger area in the matrix compared to without diffusion. Therefore, diffusion helps to control the CO_2 to flow back in the well and result in lower produced GOR.

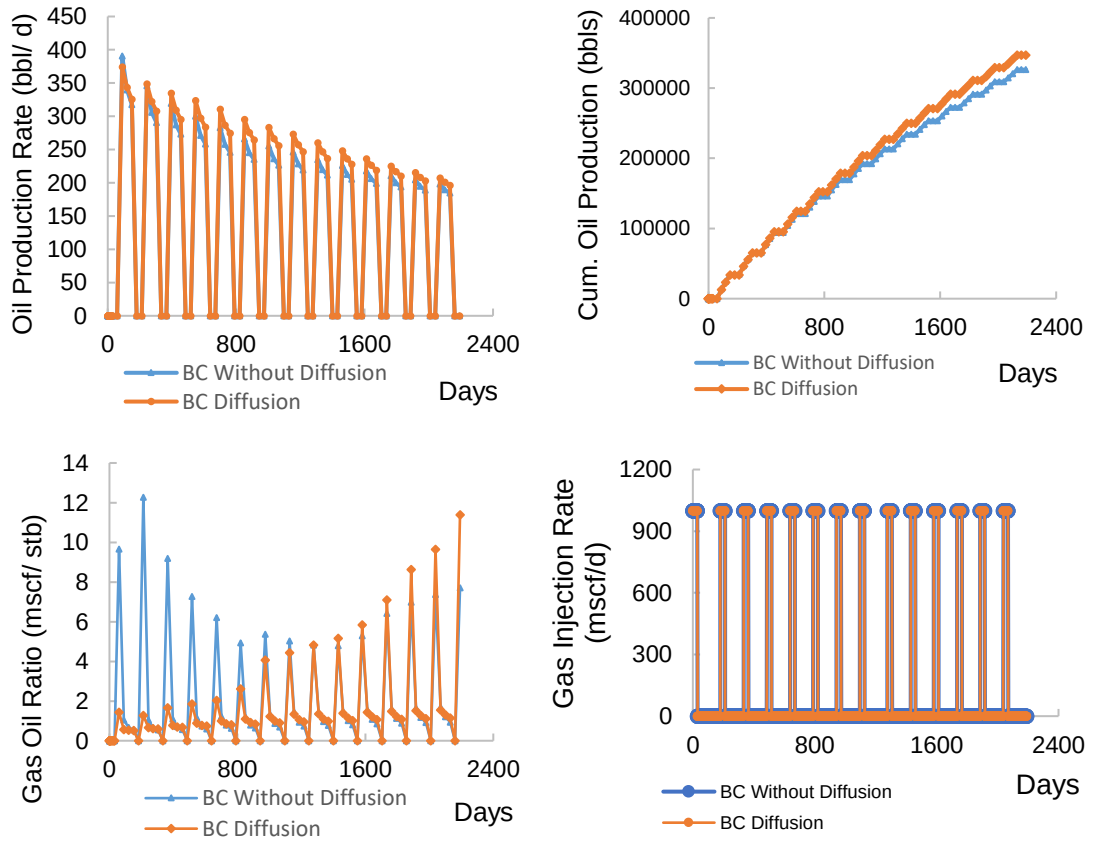
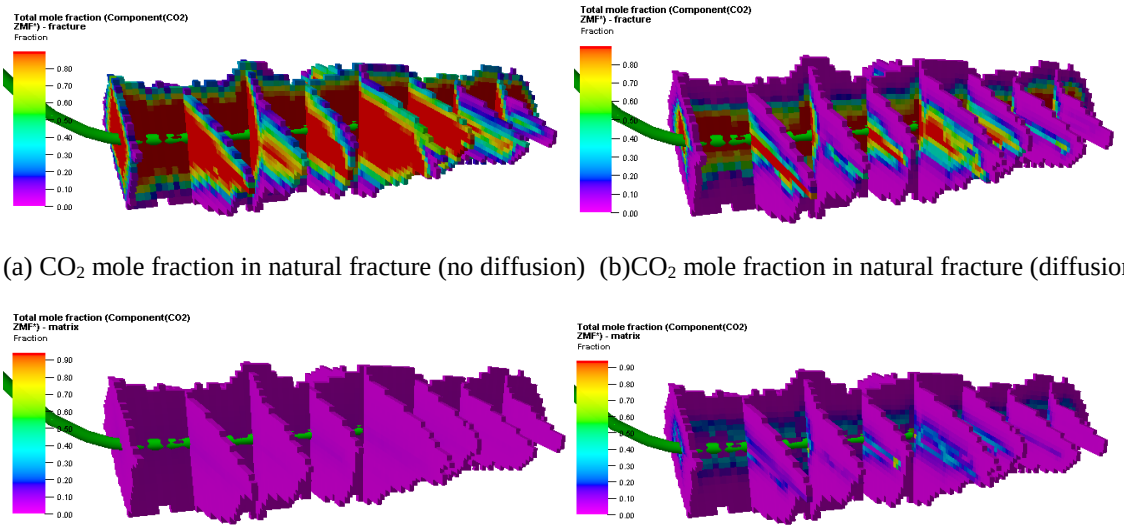


Figure 20. Well-performance comparison between diffusion and without diffusion.

More interestingly, CO_2 total mole fraction distribution was observed in both matrix (**Figure 21 c, d**) and natural fracture (**Figure 21 a, b**) systems. These representations in this figure are the distribution at the end of the soaking period of the first cycle to contrast between them. It is clearly observed that diffusion (**Figure 21 b, d**) allows more CO_2 to spread over the larger area in the matrix and less space in the natural fracture compares to without diffusion (**Figure 21 a, c**).



(a) CO_2 mole fraction in natural fracture (no diffusion) (b)CO_2 mole fraction in natural fracture (diffusion)

(c) CO_2 mole fraction in matrix (no diffusion) (d) CO_2 mole fraction in matrix (diffusion)

Figure 21. Comparison of CO_2 distribution in matrix and natural fracture between diffusion and no diffusion effect.

Determining the minimum miscibility pressure (MMP) is crucial in CO_2 miscible flood. Correlations are typically used to estimate the MMP in the absence of experimental works. For the given in-situ fluid composition and reservoir conditions, a variety of correlations developed by Cronquist (1977), Holm and Josendal (1982), Metcalfe (1982), Glaso (1985), and Yuan et al. (2004) were applied in this study. Most correlations in the literature estimate the MMP as a function of reservoir temperature and composition of reservoir fluid. While Metcalfe (1982)

stated that there is little or no effect of fluid composition on MMP, Holm and Josendal (2012) found the linear function of MMP to the amount of C_5 to C_{30} components. Details of these correlations are mentioned in the Appendix section. In **Table 11**, we normalized C_{5+} mole fraction from original compositions in order to estimate the MMP.

Table 11. Normalized C_{5+} mole fraction for MMP model.

	Mole fraction	Molecular weight	Mole weight	Normalized mole fraction	Mole weight
C5	0.101	72.2	7.29	0.151	10.86
C6	0.074	86.2	6.38	0.110	9.50
C7+	0.496	216	107.14	0.739	159.67
Total	0.671		120.81	1	180.03

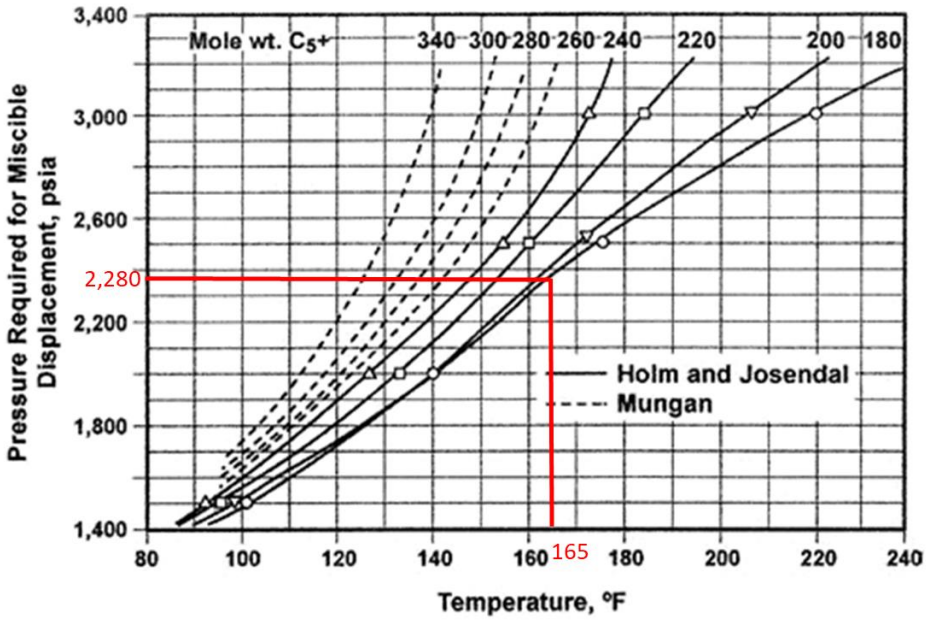


Figure 22. MMP estimation using Holm and Josendal method (modified from Jarrell et al., 2012)

Then, **Figure 22** provides the MMP value approximately of 2,280 psia using Holm and Josendal method. Further correlations provide the complete MMP result showing clearly in **Table 12**. Estimated MMP values range from 2,027 psia to 2,403 psia at reservoir temperature of

165 ^{o}F. In addition, from literature review, Adel et al. (2018) recently conducted their experiments for CO_2 injection in shale using crude oil and core plug from Wolfcamp. Their determination of CO_2 MMP by slim-tube method was 1,925 psig at 155 ^{o}F. Assuming the same temperature condition as in their slim-tube test, MMP values from the correlations are between 1,910 psia and 2,250 psia. Therefore, MMP estimation from proposed correlations is considerably accurate for interpretation of simulation results.

Table 12. MMP Results Using Various Correlations

MMP (psia) using different correlations				
Holm and Josendal (1982)	**Cronquist (1977)**	**Metcalfe (1982)**	**Glaso (1985)**	**Yuan et al. (2004)**
2,280	2,027	2,066	2,065	2,403

From simulation results, pressure in the near wellbore regions change significantly through 14 cycles of huff-n-puff as reservoir depletion occurs (Figure 38 in Appendix). Pressure remains high in the first 4 cycles of injection periods, likely 4,000 psia and above. However, once the well comes into production, pressure in the innermost region drops to below 2,500 psia. In these cycles, pressure in the outer regions remains high at proximately 3,200 psia and above. Once the huff-n-puff passes 10 cycles, the pressure increases due to injection compensate the loss due to reservoir depletion carrying from the previous production periods. Hence, injection reaches at about 2,800 psia in the injection periods and continuous to decrease in the following cycles. In production period, larger area was observed with pressure less than 2,000 psia.

In gist, for early injection cycles of the huff-n-puff scheme in our simulation models, the pressure levels are above the MMP. Also, local miscibility will occur in some areas of the stimulated reservoir volume at later injection cycles as well. Pressure behaves differently from closest region near the wellbore to the outermost region, and it decreases through the later cycles.

So, the behavior occurred at both above and below MMP conditions in the production states depending on cycle length and how far of the region to the well lateral.

4.2 Sensitivity in Reservoir Quality

This section discusses the simulation results of CO_2 huff-n-puff in unconventional reservoirs under different scenarios of reservoir quality in term of porosity and permeability as described in Chapter 2. As mentioned in **Table 10**, Case 1, Case 5 and Case 9 represent for moderate, low and high reservoir quality without diffusion effect, respectively. The same reservoir quality scenarios correspond to Case 2, Case 6, and Case 10, but with diffusion impacts. As a result, **Figure 23** exhibits production performance in oil rate and cumulative oil for these scenarios. It can be obviously seen that high reservoir quality case with diffusion (Case 10) creates the maximum production among defined cases, while low reservoir quality without diffusion case (Case 5) yields the lowest numbers. The incremental recovery statistics is presented in **Table 13**, where the base case is established as Case 1.

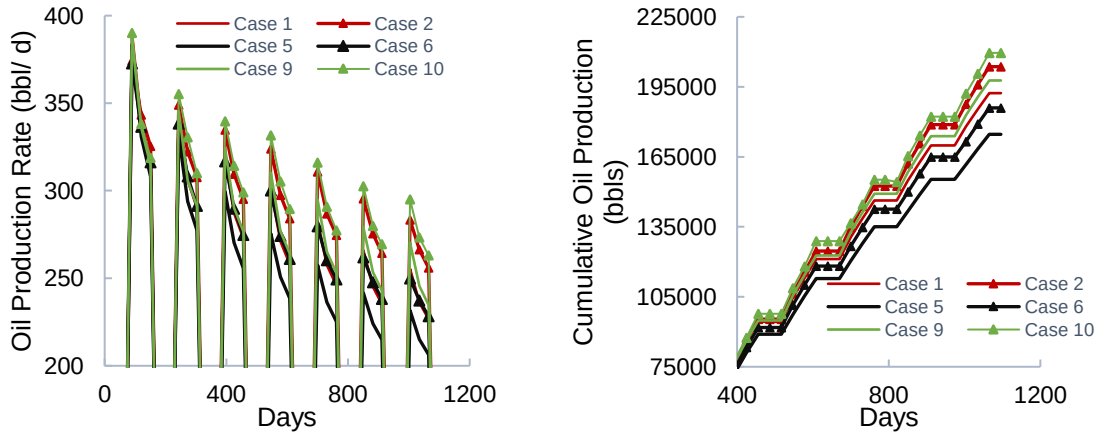


Figure 23. Huff-n-puff simulation results of different scenarios of reservoir quality and diffusion.

Table 13. Incremental oil recovery for cases at different reservoir qualities.

Case Number	Case Description	Incremental Recovery compares to Case 1 (%)
Case 1	Base case without diffusion	-
Case 2	Base case with diffusion	6
Case 5	Low reservoir quality without diffusion	-9
Case 6	Low reservoir quality, with diffusion	-3
Case 9	High reservoir quality without diffusion	3
Case 10	High reservoir quality with diffusion	9

Additionally, production stream for different components were tracked, and for the brevity, **Figure 24** displays for CO_2 and heavy component hydrocarbon (C_{7+}) only. Simulation results for other lumped components are displayed in the Appendix section at the end of this report. Results from these simulation cases indicate the most production of heavy hydrocarbon components from high reservoir quality scenario (Case 10). This outcome is completely consistent with previous analysis displayed in **Figure 23** as total production is mostly contributed from heavy hydrocarbon components (C_{7+}). Besides, CO_2 production in low reservoir quality scenario was found greatest one.

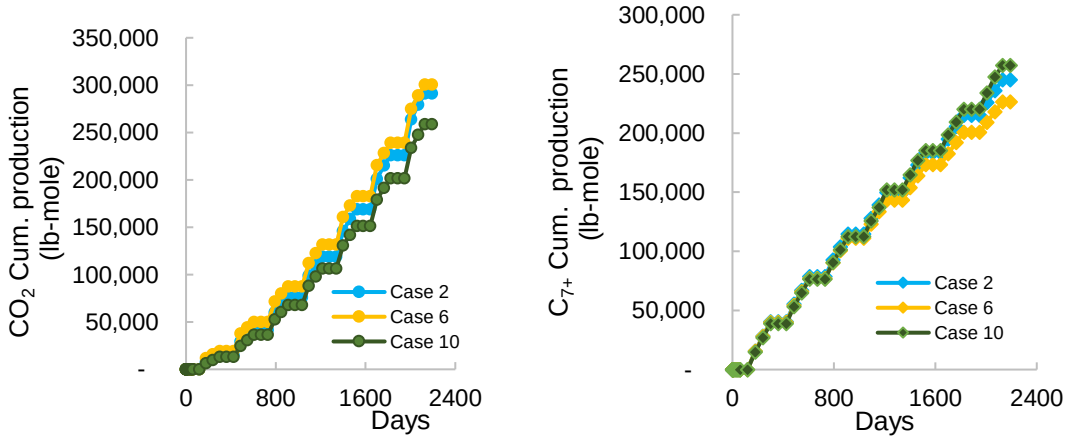


Figure 24. Component production stream (CO_2, C_{7+}) comparison for different reservoir quality cases.

4.3 Sensitivity in Diffusion Coefficient

This section presents and compares simulation results from various diffusion cases while maintaining the same reservoir quality for the consistency. There was interestingly no significant incremental oil recovery observed among these cases. Hence, by contrasting the production stream would be provide some insights about the impact of diffusion intensity on individual components. **Figure 25** depicts the CO_2 and C_{7+} mole production for explored cases. As described in **Table 10**, Case 1 represents for moderate reservoir quality without diffusion. The same reservoir quality scenario but with medium, low, and high diffusion coefficients are represented in Case 2, Case 3, and Case 4 respectively. The separation in produced CO_2 is clearly observed among these cases, especially when distinguishing from Case 1 to the remaining cases. Interestingly, more CO_2 was produced back in the well in high diffusion scenario (Case 4) comparing to medium and low scenarios (Case 2 and Case 3). In addition, C_{7+} are likely the same in all diffusion cases which resulted in insignificant incremental oil recovery among low, medium and high diffusion cases. For clarity, **Table 14** shows the percentage production variation (in lb-mole) departing from the base case.

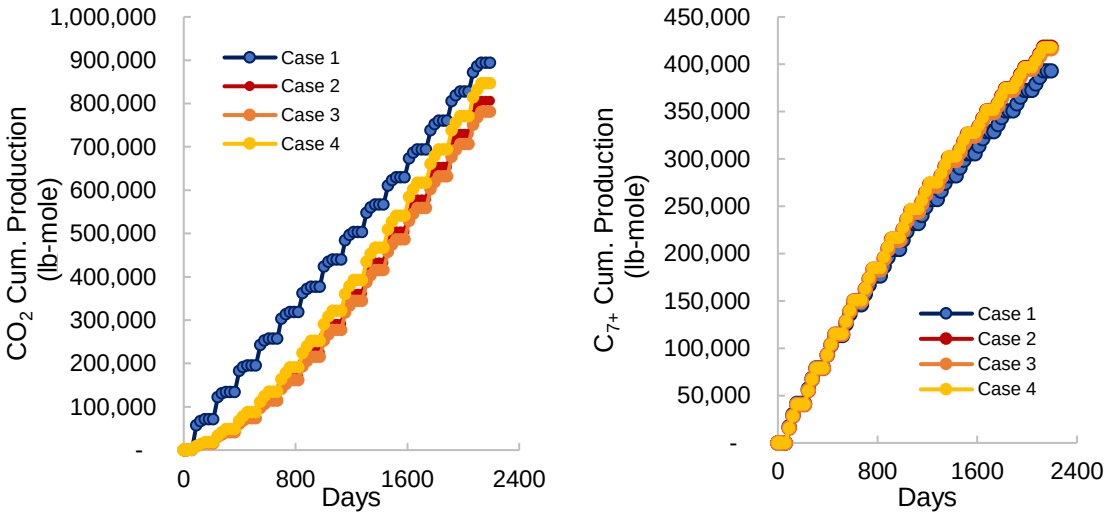


Figure 25. Component-production stream (CO_2, C_{7+}) comparison for different diffusion-coefficients cases.

Table 14. Variation in production (lb-mole) for different diffusion-coefficients cases.

Case Number	Case Description	% Difference in produced CO_2 compared to Case 1	% Difference in produced C_{7+} compared to Case 1
Case 1	Moderate reservoir without diffusion	-	-
Case 2	Moderate reservoir with mid diffusion	-10	6
Case 3	Moderate reservoir with low diffusion	-13	6
Case 4	Moderate reservoir with high diffusion	-5	6

Chapter 5: Compositional Variation

This section presents the simulation results of typical thermophysical properties such as CO_2 total mole fraction, methane total mole fraction, and heavy hydrocarbon components total mole fraction associating with the departure in pressure, oil saturation, oil viscosity, and surface tension. For brevity, the evolution of these properties is illustrated through only Cycles 1, 4, 7, 11 and 14. For each full cycle, the results present at the end of the injection, soaking, and production periods. Analysis was performed by obtaining all grid cells properties in four distinct regions around the lateral horizontal well which were defined in chapter 2 of this thesis. The innermost region adjacent to the wellbore wall, Region 1, is defined with greater than 0.5 of CO_2 mole fraction. Furthermore, regions 2, 3, and 4, are stated with maximum values of CO_2 mole fraction of 0.25, 0.1 and 0.01, respectively. In terms of volume proportions, Regions 1, 2, 3 and 4 account for 8%, 17%, 35%, and 40% of total SRV, respectively.

5.1 Variation in Thermophysical Properties

The amount of CO_2 total mole-fraction retained in the rock matrix mostly represents the amount of injected CO_2 in supercritical phase at in-situ reservoir conditions. The higher the value of total mole-fraction of CO_2 in the matrix, the more favorable the mobility and the sweep efficiency being affected by the cyclic injections scheme. Histograms in **Figure 26** from the base-case reservoir model of cyclic CO_2 injection, show the distributions of CO_2 total mole fraction in SRV Region 1 of the rock matrix at the end of each selected cycle. The histograms indicate the gradual increase in the amount of CO_2 through continuous cyclic injections. For conciseness, the figures only show the most likely values of CO_2 total mole-fraction in all the subplots. **Figure 27** illustrates the same distributions of CO_2 total mole-fraction, but for all SRV regions. This outcome provides a visualization of the CO_2 total mole fraction distributions across

all the SRV regions. It appears the values in Region 1 change significantly compared to those in the outer regions.

After the first cycle, the matrix captures a minimal amount of CO_2 mole fraction of less than 0.15. However, once more cycles are performed, CO_2 dwells in the rock matrix considerably. CO_2 reaches out to Region 4 slowly and marginally in the pore matrix, occupying merely 0.02 of total mole fraction at the end of the first cycle. Then, it changes insignificantly in the following cycles, leading to only 0.07 of the total mole fractions after 14 injection cycles. Close inspection of **Figure 26** and **Figure 27** reveals distributions of CO_2 total mole fractions that are less skewed at the end of production periods compared to those for injection and soaking periods. This outcome implies a tendency toward compositional equilibration due to the molecular-diffusion process.

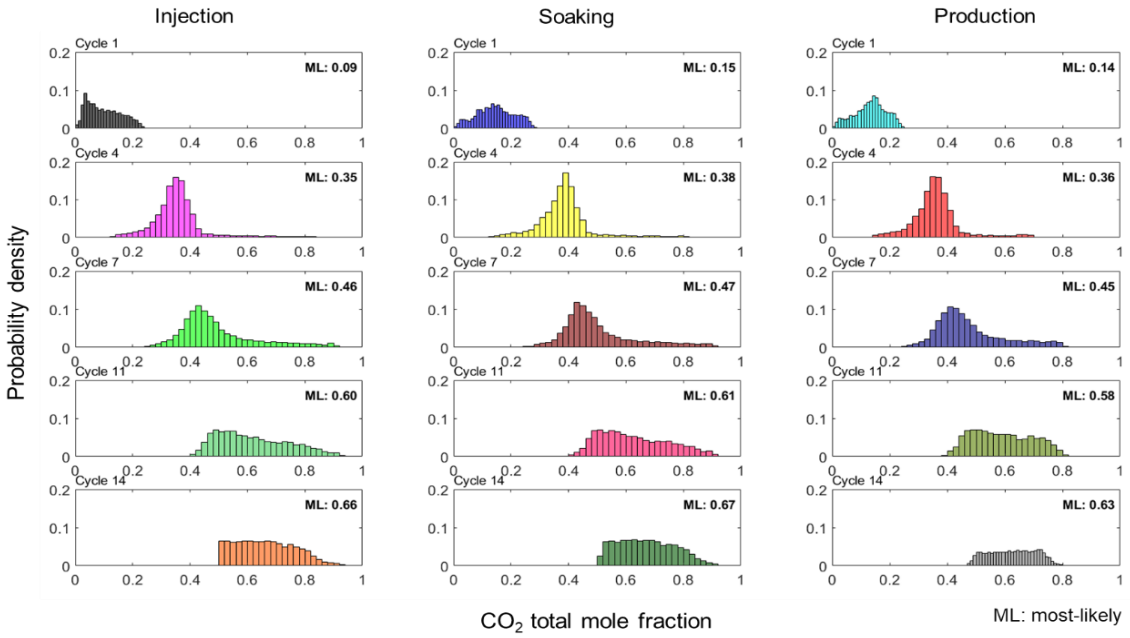


Figure 26. Evolution of total CO_2 mole fraction through selected injection cycles (SRV Region 1 only).

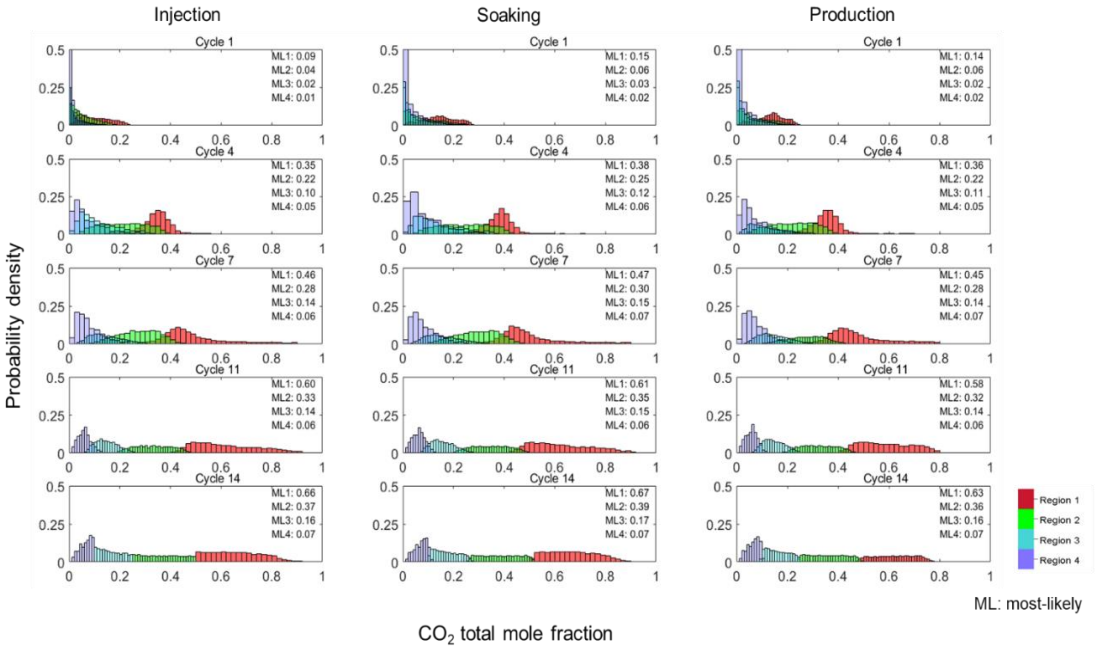


Figure 27. Evolution of CO_2 total mole-fraction through selected injection cycles (all SRV regions).

Figure 28 tracks the residual distributions of heavy hydrocarbon components (C_{7+}) over the 14 cycles. The decrease in C_{7+} liquid mole fraction over time reflects the effectiveness of the cyclic recovery process in the stimulated liquid-rich hydrocarbon reservoir well.

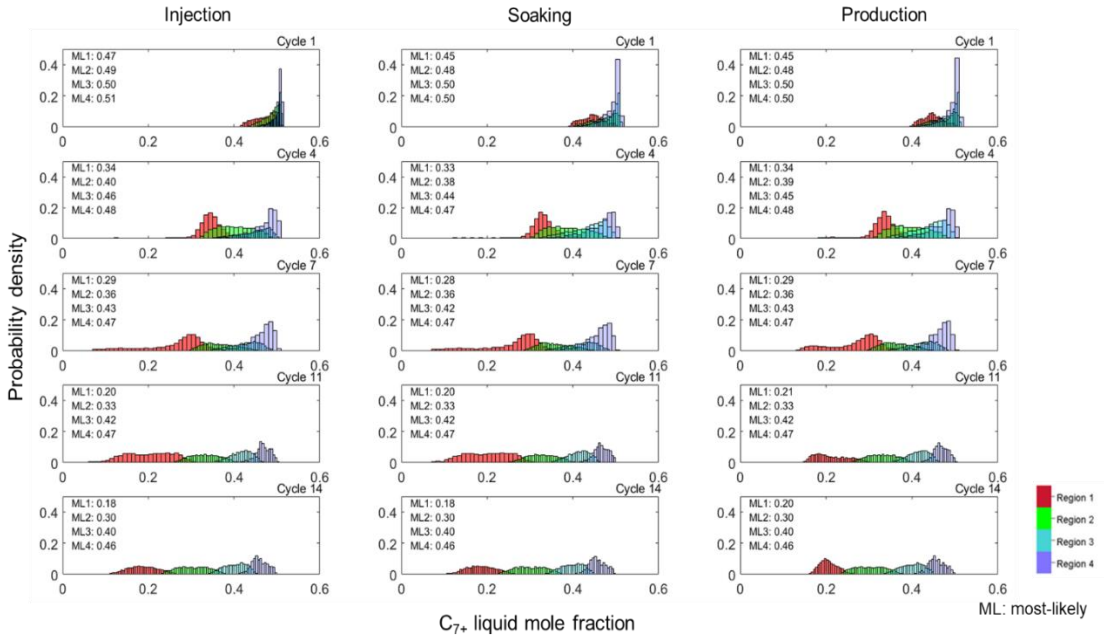


Figure 28. Evolution of liquid C_{7+} mole fraction through selected injection cycles (all SRV regions).

Before the deployment of cyclic CO_2 injection, the initial C_{7+} liquid mole fraction was approximately 0.5. At the end of the first cycle, there is only a minimal separation of total C_{7+} observed across the 4 SRV regions. It relates to slow dispersion of CO_2 into the tight matrix condition, even in SRV Region 1. Additionally, the interaction among heavier components is very restricted resulting in minimal change in C_{7+} mole fraction. Interestingly, after four cycles, the reduction in C_{7+} mole fraction becomes significant in the SRV Regions 1 and 2. The most-likely values of C_{7+} mole fractions are estimated at 0.34 and 0.38, respectively. In contrast, the mobilization of C_{7+} in the outer regions appear muted. After 14 cycles, residual C_{7+} in the matrix becomes 0.2 and 0.3 in the SRV Regions 1 and 2, respectively, while corresponding values are 0.4 and 0.46 for SRV Regions 3 and 4.

Figure 29 demonstrates similar profiles for the evolution of methane total mole-fractions. A consistent picture for methane mole fraction distributions appears as compared to the

previously discussed profiles of CO_2 and C_{7+} mole fractions. What stands out is the very narrow spread of total mole fraction of methane in the outermost region; that is, Region 4. This observation implies lightest hydrocarbon component, methane, is barely partitioning into the liquid phase away from the stimulated zones.

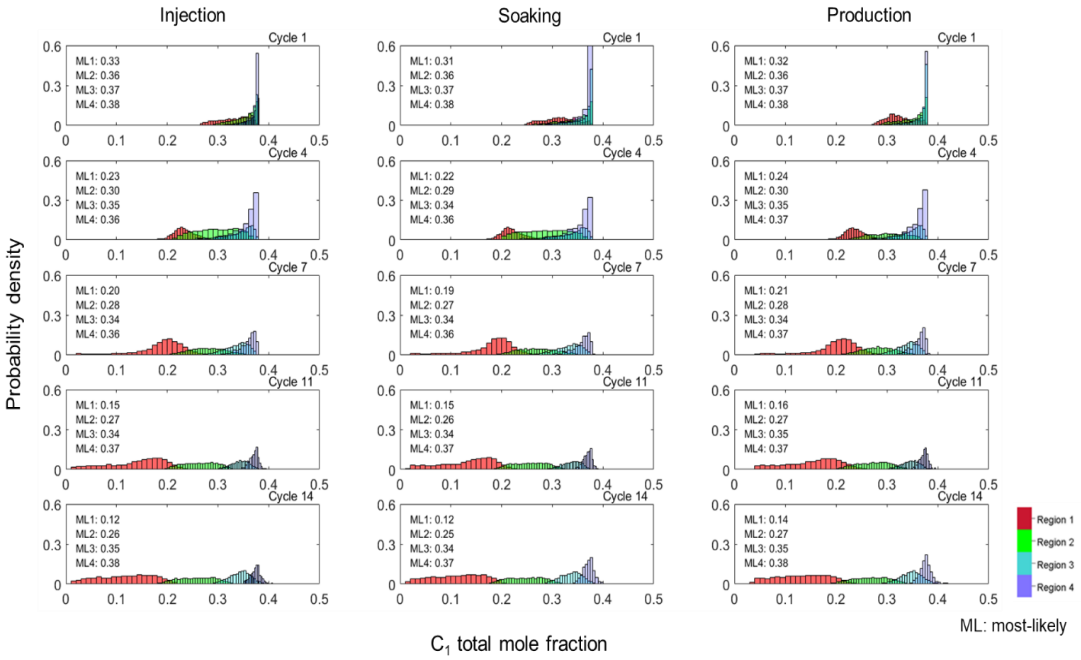


Figure 29. **Evolution of methane total mole fraction through selected injection cycles (all SRV regions).**

Figure 30 and **Figure 31** turn the attention to pressure and saturation changes over the different injection cycles, respectively. These figures plot the variance or the change in pressure and saturation from the initial pressure and saturation distributions against total mole fraction of CO_2. Thus, pressure change values are expected to be negative at the end of the early injection cycles (**Figure 30**). However, with depletion due to production, pressure variance values of later cycles become positive. This phenomenon can be observed at the end of the 4th cycle injection period. This outcome suggests the low-production life of LUR wells. The pressure variance values after the soaking cycle have less scatter because of the natural tendency of gravity-

capillary equilibrium. Pressure change values after the production periods have a much wider spread in the pressure scale. The closest grid cells around the well will deplete much faster compared to those away from the well in the outer regions. Distinct behavior of the pressure versus CO_2 mole fraction profiles across the 4-SRV regions is observed as early as the 7th cycle production period. This observation suggests that even the pressure regimes can be quite different away from the well.

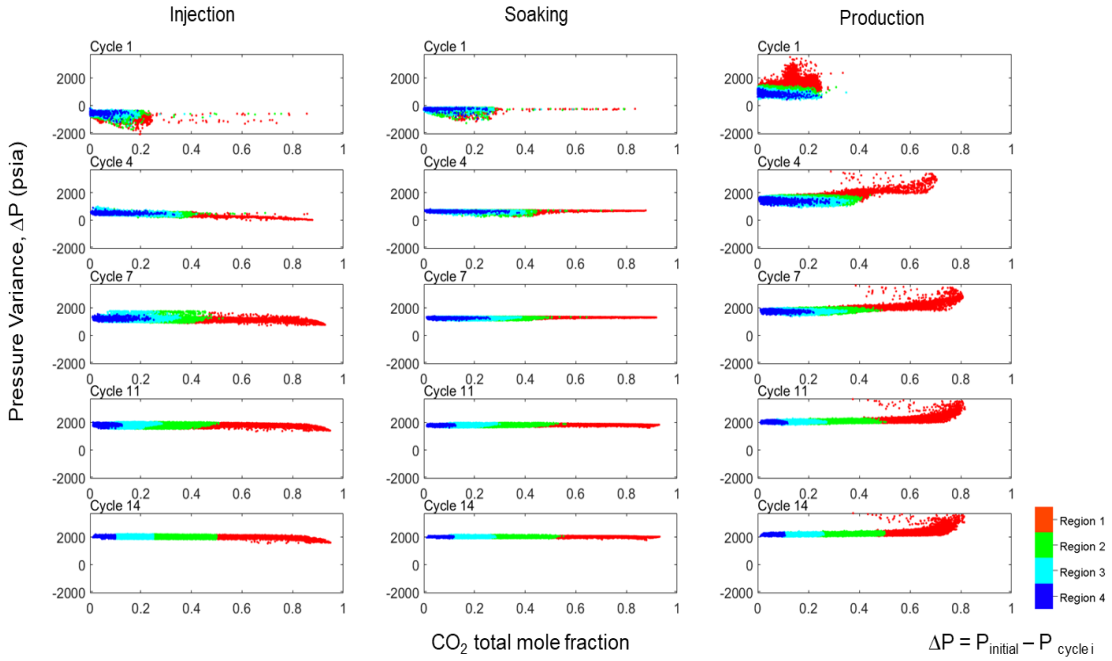


Figure 30. Evolution of pressure variation over through selected injection cycles (all SRV regions).

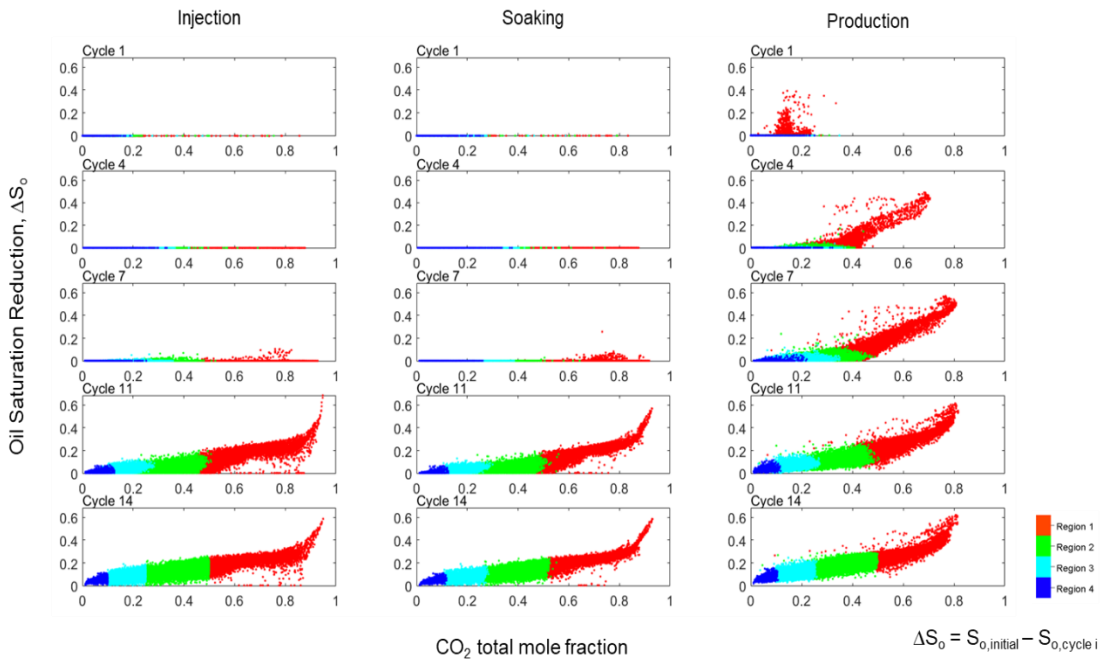


Figure 31. Evolution of reduction in oil saturation through selected injection cycles (all SRV regions).

Saturation change with the total mole fraction of CO_2 through different cycles reveals a well-matured dependency after about 10th cycle. Clear effectiveness of CO_2 injection in mobilizing the stranded oil becomes apparent particularly at the end of the production periods.

In any solvent injection process, one of efficiency metrics will be the degree of viscosity reduction of the oil under in-situ conditions with solvent injection. Conducted work includes examining the viscosity reduction versus CO_2 mole fraction with the injection cycles in **Figure 32**. The initial oil viscosity is 2 cp under in-situ conditions prior to any injection. A distinctly clear relationship emerges for the viscosity reduction profiles from as early as the first cycle production period. As expected, increasing CO_2 content results in lower oil viscosity.

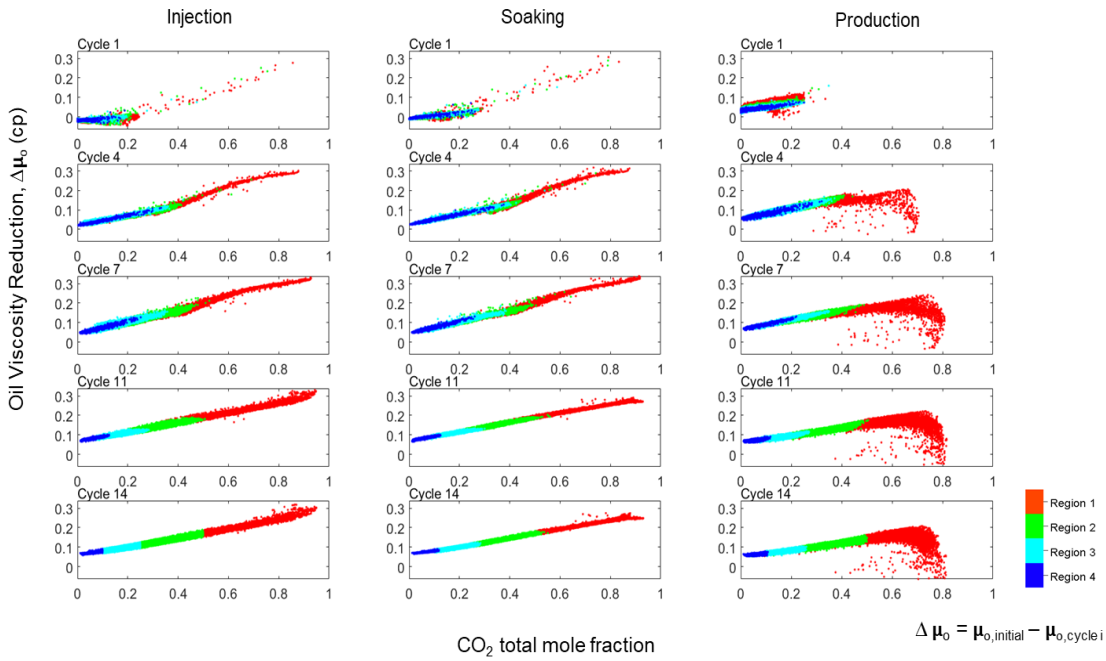


Figure 32. Evolution of oil viscosity reduction through selected injection cycles (all SRV regions).

Figure 33 presents another important thermophysical property–surface tension between oil and gas. The figure plots oil/vapor surface tension against total mole-fraction for the injection cycles. As the pressure decreases with production, the vapor phase emerges in the in-situ reservoir conditions. Surface tension values will be non-zero once the vapor phase appears, which the figure shows. Also observed in this figure, is the reduction in the surface tension values as the CO_2 content increases. Reduction in surface tension reflects the attainment of more favorable miscibility condition. The oil becomes lighter with increasing CO_2 in a liquid state. As for the spatial distribution of the surface tension, more scatter is evident in SRV Region 1 compared to outer regions. By the end of the 14th cycle, almost all the grid cells in all the SRV regions show the presence of both oil and vapor phase.

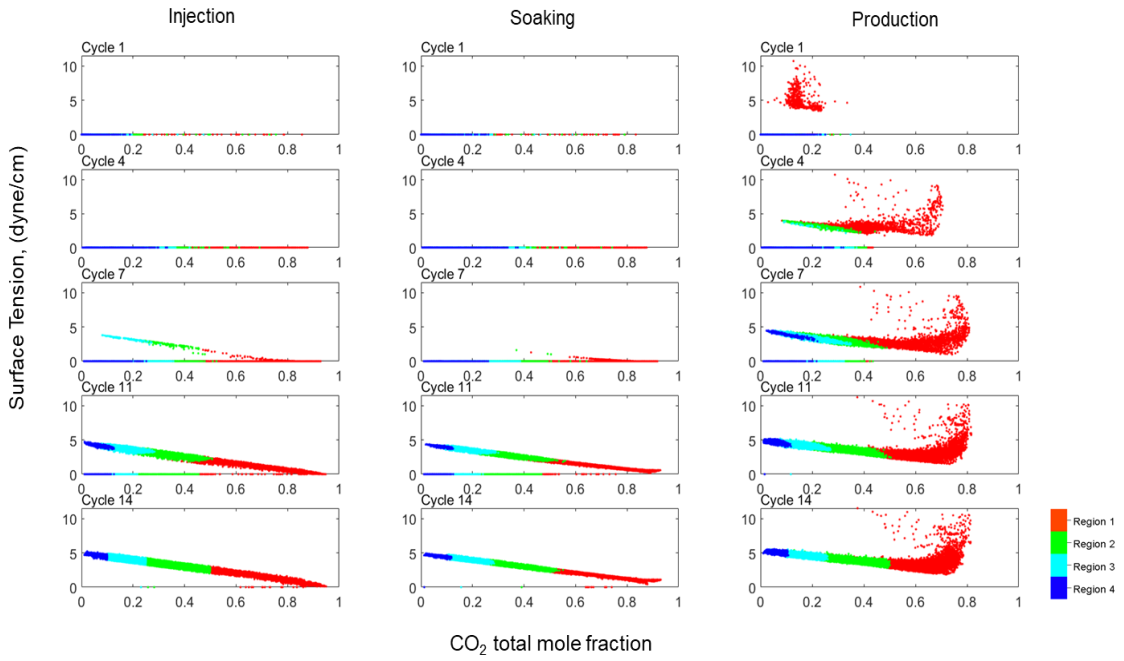


Figure 33. Evolution of oil-vapor surface tension through selected injection cycles (all SRV regions).

5.2 Contacted CO_2 Volumes and CO_2 Retention in the Porous Media

Figure 34 presents how efficiently CO_2 spatially disperses into the rock matrix through 14 cycles. Without molecular diffusion, CO_2 spreads over only 2% of stimulated HCPV toward the matrix in the first cycle. Hence, most of the injected CO_2 during the injection period remains in the hydraulic-fracture and pre-existing natural fracture networks. Once the well is brought back on production, this mobile CO_2 quickly flow back into the wellbore resulting in excessive initial GOR as depicted in **Figure 20** previously. On the other hand, more CO_2 breaks into the matrix through all cycles of cyclic CO_2 injection due to diffusion. It turns out that approximately 90% hydraulic fracturing stimulated Hydrocarbon Pore Volume (HCPV) in the matrix is filled-up with injected CO_2 in the diffusion case compared to only 60% without diffusion consideration.

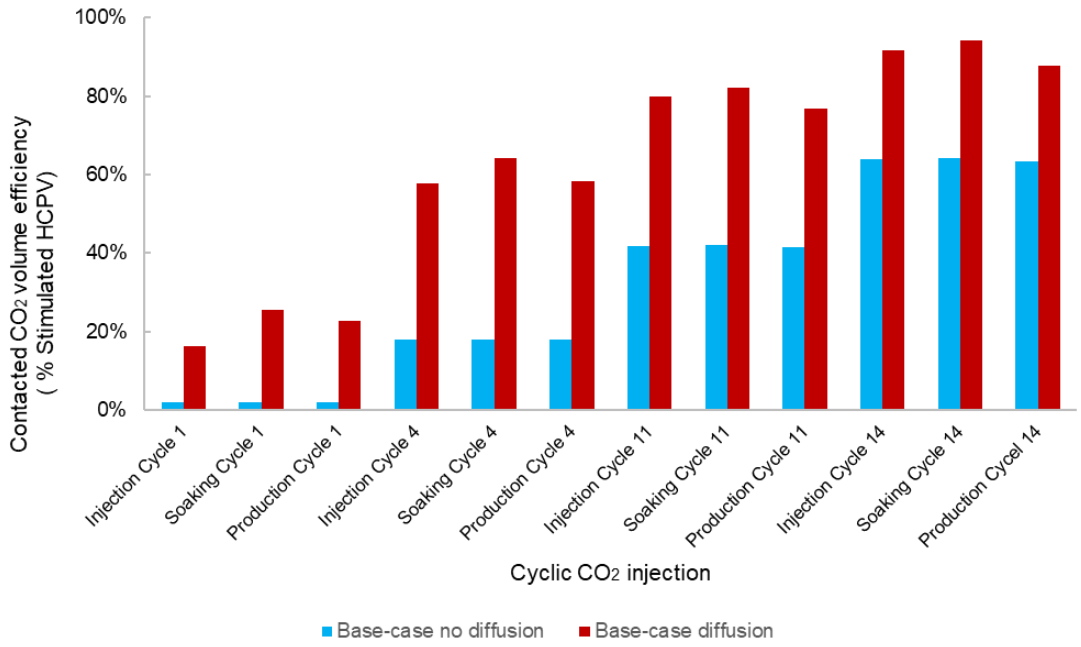


Figure 34. CO_2 diffusion efficiency into the rock matrix of the SRV.

Additionally, a crucial measure in any CO_2 EOR or sequestration is how much CO_2 would have been captured in the reservoir, named CO_2 retention. Larger CO_2 retention rate in the reservoir permits further miscibility, mobility effect, and sweep efficiency. I defined the CO_2 retention rate as displayed in **Eq. 7** and illustrating the CO_2 retention rate through all cycles of the huff-n-puff for base case without diffusion (Case 1) and with diffusion (Case 2) in **Figure 35**. It can be seen that diffusion captures more CO_2 in the rock matrix through all cycles. Especially, more than 50% of injected CO_2 was stored in the reservoir in the first 1,000 days of huff-n-puff operations with diffusion impact, while this number is approximately 30% in without diffusion.

$$\mathrm{CO_2\,Retention\ Rate} = \frac{CO_2\ injected - CO_2 produced}{CO_2\ injected} \tag{7}$$

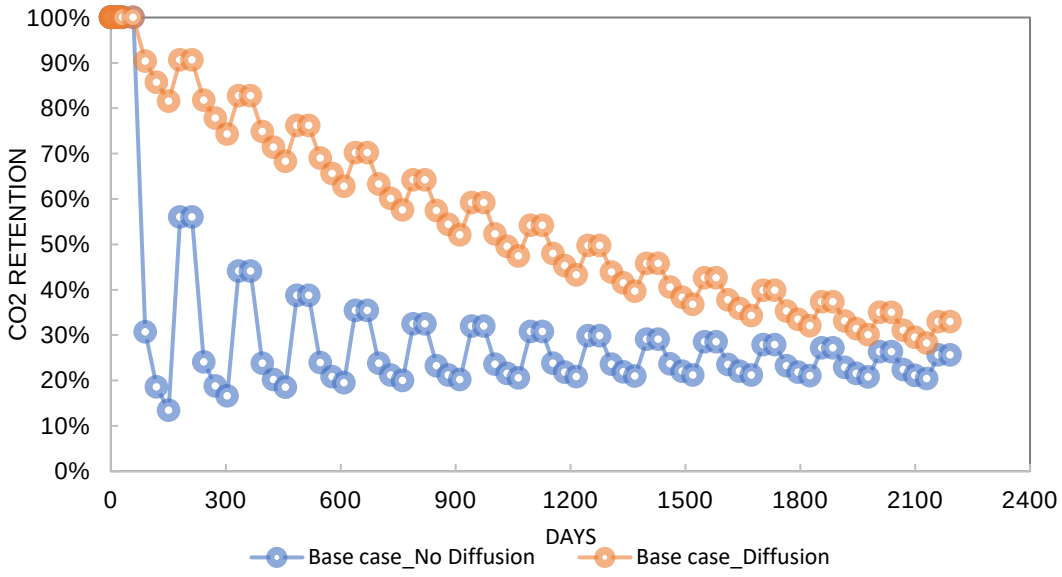


Figure 35. CO_2 retention rate through huff-n-puff injection. Diffusion captures more CO_2 retained in the rock matrix

Chapter 6: Discussions, Limitations and Future Work

The integrated workflow presented in this Chapter 2 requires full range of data to construct the model for unconventional liquid reservoirs. Although limited number of wells and public data were used, it offered robust steps and comprehensive methods in achieving realistic reservoir characterization and detailed fracture network. These crucial features had been simplified or ignored in many previous studies. In future work, more available wells and geochemical data would create more realistic Wolfcamp reservoir structures and reduce the uncertainty in properties estimation.

Several assumptions have been made in the simulation models:

- Regional 3D geological and earth models were constructed based on limited available well data
- Empirical correlations used to compute Young Modulus and Poisson's ratio
- Impact of natural fracture to hydraulic fracture propagation was negligible
- Fix huff-n-puff design for injection rate, cycle length was assumed to be constant through cycles

Although accurate fracture network and its properties such as fracture width, half-length and conductivity were created using commercial 3D fracture simulator GOHFER, coupling them into 3D reservoir simulator has never been a plain task for accurate modeling purpose. The consistent grid system was both used in 3D fracture simulator and 3D reservoir simulator ECLIPSE. Our grid size of 20 ft × 20 ft × 5 ft might not capture the complexity of induced fractures and fluid flow occurred within 20 ft length. This means that grid size would need to be much smaller to properly model the flow in the fracture system. However, it obviously requires more computational effort and beyond out of my scope in this study. In addition, the

transmissibility multipliers used in this study from the conversion of fracture conductivity appears to be less than ideal.

The single well with multi-stages induced fractures was assumed while disregarding the interference or any flowing effect from offset wells. It can be explained by the main objective. It aims for huff-n-puff process where injection and production period are occurred in the same well. Also, the analysis was defined for nearby area around the lateral well. Moreover, the attention of molecular diffusion flow occurs only limited space beyond the lateral given simulation times and allowed computational efforts. Practically, multi-wells in the same pad should be more relevant to be considered in the model once wells with small spacing from 200 ft to 500 ft are drilled in recent years. In that case, gas breakthrough likely occurs early in the offset wells once huff-n-puff is implemented.

Two independent systems including fracture and matrix were defined in all grid cells along with populated rock and fluid properties. Dual-porosity system was used rather than dual-permeability where I assumed flowing occurs either from natural fracture to well or matrix to fracture. Flowing in horizontal wells is mainly contributed directly from induced fractures during the hydraulic fracturing stages. Later, fluid in the matrix will migrate toward fractures with less significant production impact. Future work to implement dual-permeability will provide more insights of the fluid flow from matrix directly to the well.

Diffusion in both oil and gas phases was utilized for all components. Although various diffusion coefficients were modeled to capture the significant impact due to pressure change during the huff-n-puff operations, there would be more accurate approach if diffusion coefficients were established as a function of pressure, time and mole fraction of specified components. The cross phase diffusive flow might be important in this huff-n-puff flow.

However, the mechanism in cross phase diffusion probably takes slower diffusion than the one that has been investigated. Another approach can be considered for the future work using activity corrected diffusion coefficients instead of normal diffusion coefficients.

All simulation results presented in Chapter 4 and Chapter 5 were modeled using a fixed huff-n-puff design and process. One huff-n-puff cycle design includes 1 month of injection, followed by 1 month of soaking, and 3 months of production. This short cycle length allowed more cycles had been scheduled over a reasonable simulated time frame of investigation and computational constraints. Furthermore, extended cycle such as 2 months of soaking, injection and 6 months of production would be a worthy alternative to understand the diffusion impact on the huff-n-puff compares to the mentioned cases.

Chapter 7: Conclusions

Using a holistic integrated workflow, comprehensive hydraulically fractured wells in liquid-rich unconventional reservoirs (LUR) were modelled to apply for Midland Basin. The approach incorporates relevant geological, petrophysical, mineralogical, geomechanical and hydraulic-fracturing data, measurements and information and engineering practices. Employing multi-component compositional simulation and accounting for both convective and diffusive (pressure and molecular) flow, the authors critically examine the inner dynamics of the stimulated regions around hydraulically fractured wells. Evolution of thermophysical properties in these wells undergoing cyclic-CO2 injection reveals occurrence of interesting and complex physical processes. In addition, this investigation explores the role of molecular diffusion in well performance of stimulated LUR wells and attempts to explain how, when, and where various physical processes occur inside these LUR wells.

This study paves the way for the following findings:

1. Modeling the molecular diffusion effect becomes essential to accurately evaluate the recovery performance of hydraulically fractured LUR wells undergoing cyclic CO_2 injection. Molecular diffusion can account for more than 6% incremental recovery in 6 years of cyclic injection.
2. Several injection cycles for the solvent (CO_2) injection process becomes a requirement before the process becomes optimally effective. In other words, early sequences may not yield incremental recovery.
3. The evolution of thermophysical properties reveals distinct spatial patterns may develop around the stimulated LUR wells. Average CO_2 total mole-fraction in rock matrix in the innermost region increases to 0.63 in 6 years (after 14 cycles) whereas the corresponding

increase in the following areas is merely 0.36, 0.16 and 0.07, respectively. These numbers, of course, may vary slightly depending on the reservoir properties and operating conditions.

4. Pressure regimes can be entirely different away from the well. Saturation change with total mole-fraction of CO_2 through different cycles reveals a well-matured dependency after about 10^{th} cycle.
5. A clear relationship may emerge for the oil-viscosity reduction profiles with CO_2 total mole-fraction from as early as the first cycle production period. By the end of the 14^{th} cycle, almost all the grid cells within SRV regions show the presence of both oil and vapor phase.
6. Injected solvent (CO_2) can diffuse into approximately 90% of hydraulically fractured stimulated HCPV in the rock matrix within 14 cycles.

Nomenclature

E	Young's modulus, psia
D	diffusion coefficient, m^2/s
J_i	molar diffusion flux, $m^{-2}s^{-1}$
M	molecular weight, g/ mol
P	pressure, psia
T	temperature, ^oF
V_p	compressional wave velocity, ft/s
V_s	shear wave velocity, ft/s
X_f	fracture half-length, ft
ν	Poisson's ratio
μ	viscosity, cp
σ	surface tension, dyne/cm

References

Alfarge, D., Alsaba, M., Wei, M., & Bai, B., 2018. Miscible Gases based EOR in Unconventional Liquids Rich Reservoirs: What We Can Learn. International Heavy Oil Conf. & Exh. 10-12 December, Kuwait City. doi:10.2118/193748-MS

Alfarge, D., Wei, M., Bai, B., 2017. IOR Methods in Unconventional Reservoirs of North America: Comprehensive Review. SPE West. Reg. Meet. https://doi.org/10.2118/185640-MS

Alimahomed, F., Malpani, R., Jose, R., Haddad, E., Arteaga, E. V, Smith, L., Lati, S., 2017. SPE-187496-MS Stacked Pay Pad Development in the Midland Basin.

Approach Resources, 2010. Investor & Analyst Meeting Forward-looking statements.

Barree & Associates, 2017. Gohfer 3D User Manual.

Beard, T., 2011. EPA Hydraulic Fracturing Workshop March 10 th - 11 th , 2011 " Fracture Design in Horizontal Shale Wells – Data Gathering to Implementation ."

Blomquist, P.K., 2016. Wolfcamp Horizontal Play , Midland Basin , West Texas * 10890.

Castagna, J.P., Batzle, M.L., Eastwood, R.L., 1984. Relationship Between Compressional and Shear-wave Velocities in Classic Silicate Rocks. SEG Tech. Progr. Expand. Abstr. 1984 50, 582–584. https://doi.org/10.1190/1.1894108

Cronquist, C. , 1977. Carbon Dioxide Dynamic Miscibility with Light Reservoir Oils. 4th U.S. DOE Symposium, Tulsa, 1977.

EIA, 2018. Major U.S. Tight Oil-Producing States Expected to Drive Production Gains Through 2018. U.S. Energy Inf. Adm.

Encana, 2015. ENCANA CORPORATION Permian Basin Presentation Focus and Efficiency Driving Quality Returns Encana ' s R & D Lab Is In The Field 1–12.

Fairhurst, B., Hanson, M.L., Reid, F., Pieracacos, N., 2012. WolfBone Play Evolution , Southern Delaware Basin : Geologic Concept Modifications That Have Enhanced Economic Success * 10412.

Gale, J.F.W., Laubach, Stephen Ernest, Olson, J.E., Laubach, Stephen E, Olson, J.E., Eichhubl,

P., Fall, A., 2015. Natural Fractures in shale : A Review and New Observations. https://doi.org/10.1306/08121413151

Glaso, O. 1985. Generalized Minimum Miscibility Pressure Correlation. SPEJ 927-934, Dec. 1985.

Gupta, I., Rai, C., Sondergeld, C., Devegowda, D., 2017. Rock typing in Wolfcamp Formation. SPWLA 58th Annu. Logging Symp. https://doi.org/10.1097/01.mao.0000185066.04834.4e

Hamlin, H.S., Baumgardner, R.W., 2012. Wolfberry Play , Midland Basin , West Texas . AAPG Southwest Section Meeting, Ft. Worth, TX #10419.

Hawthorne, S.B., Gorecki, C.D., Sorensen, J.A., Steadman, E.N., Harju, J.A., Melzer, S., 2013. Hydrocarbon Mobilization Mechanisms from Upper, Middle, and Lower Bakken Reservoir Rocks Exposed to CO. SPE Unconv. Resour. Conf. Canada. https://doi.org/10.2118/167200-MS

Henry, J., 2012. " Wolfberry "— Wolfcamp / Spraberry : How It Started * 110164.

Hirschfelder, J.O., Byron Bird, R., Spotz, E.L., 1949. The Transport Properties of Gases and Gaseous Mixtures. II. Chem. Rev. 44, 205–231. https://doi.org/10.1021/cr60137a012

Hoffman, B.T., 2018. Huff-n-Puff Gas Injection Pilot Projects in the Eagle Ford. SPE Canada Unconv. Resour. Conf. 13-14 March, Calgary, Alberta, Canada. doi:10.2118/189816-MS.

Hoffman, B. T., Evans, J. G., 2016. Improved Oil Recovery IOR Pilot Projects in the Bakken Formation. SPE Low Perm Sym., 5-6 May, Denver, Colorado, USA. doi:10.2118/180270-MS

Holm, L. W. and Josendal, V. A., 1980. Effect of Oil Composition on Miscible-Type Displacement by Carbon Dioxide. 1st SPE/ DOE Symposium on EOR, Tulsa, OK, Apr-1980, SPE 8814.

Jacobs, T., 2017. Oil and Gas Producers Find Frac Hits in Shale Wells a Major Challenge. J. Pet. Technol. 69, 29–34. https://doi.org/10.2118/0417-0029-JPT.

Jarrell, P.M., Fox, C., Stein, M., and Webb, S., 2002. Practical Aspects of CO2 Flooding. SPE Monograph SeriesVol 22, 214

Jaripatke, O.A., Barman, I., Ndungu, J.G., Schein, G.W., et al. 2018. Review of Permian Completion Designs and Results. SPE Annual Tech. Conf. & Exh. 24-26 September, Dallas, Texas, USA. https://doi.org.ezproxy.lib.uh.edu/10.2118/191560-MS.

Kvale, E.P., Rahman, M.W., Energy, D., 2016. Depositional Facies and Organic Content of Upper Wolfcamp Formation (Permian) Delaware Basin and Implications for Sequence Stratigraphy and Hydrocarbon Source.

Metcalfe, R.S. 1982. Effect of Impurities on Minimum Miscibility Pressures and Minimum Enrichment Levels for CO_2 and Riched-Gas Displacement. SPEJ, 219-225, Apr. 1982.

Miskimins, J., Graves, R., Hurley, N., Barree, R., 2002. Extrapolation of Rock Mechanical Properties From a Cored Well to an Uncored Well Through the Use of Electrofacies. SPE/ISRM Rock Mech. Conf. https://doi.org/10.2118/78250-MS

Ojha, S.P., Misra, S., Sinha, A., Dang, S., Tinni, A., Sondergeld, C., Rai, C., 2017. SPE-187398-MS Relative Permeability and Residual Saturation Estimates for Organic-Rich Shale Samples From Bakken , Wolfcamp , Eagle Ford and Woodford Formations.

Renner, T.A., 1988. Measurement and Correlation of Diffusion Coefficients for CO2 and Rich-Gas Applications. SPE Reserv. Eng. 3, 517–523. https://doi.org/10.2118/15391-pa

Shelokov, V., Sarkar, M., Wydrinski, R., 2017. Geomechanical Facies Model for the Wolfcamp Formation (Midland Basin). Pioneer Nat. Resour. Copyr. 24–26. https://doi.org/10.15530/urtec-2017-2694220

Sheng, J.J., Cook, T., Barnes, W., Mody, F., Watson, M., Porter, M., Viswanathan, H., 2015. Screening of the EOR Potential of a Wolfcamp Shale Oil Reservoir. 49th US Rock Mech. / Geomech. Symp. 2015 2.

Whitson, C.H., Sunjerga, S., 2012. PVT in Liquid-Rich Shale Reservoirs. SPE Annu. Tech. Conf. Exhib. 8–10. https://doi.org/10.2118/155499-MS

Wickard, A.K., Elmore, R.D., Heij, G., 2016. A Diagenetic Study of the Wolfcamp Shale , Midland Basin , West Texas 1–15.

Zoback, M.D., 2007. Reservoir Geomechanics. Cambridge University Press, New York, USA.

Appendix

A1. Additional Figures

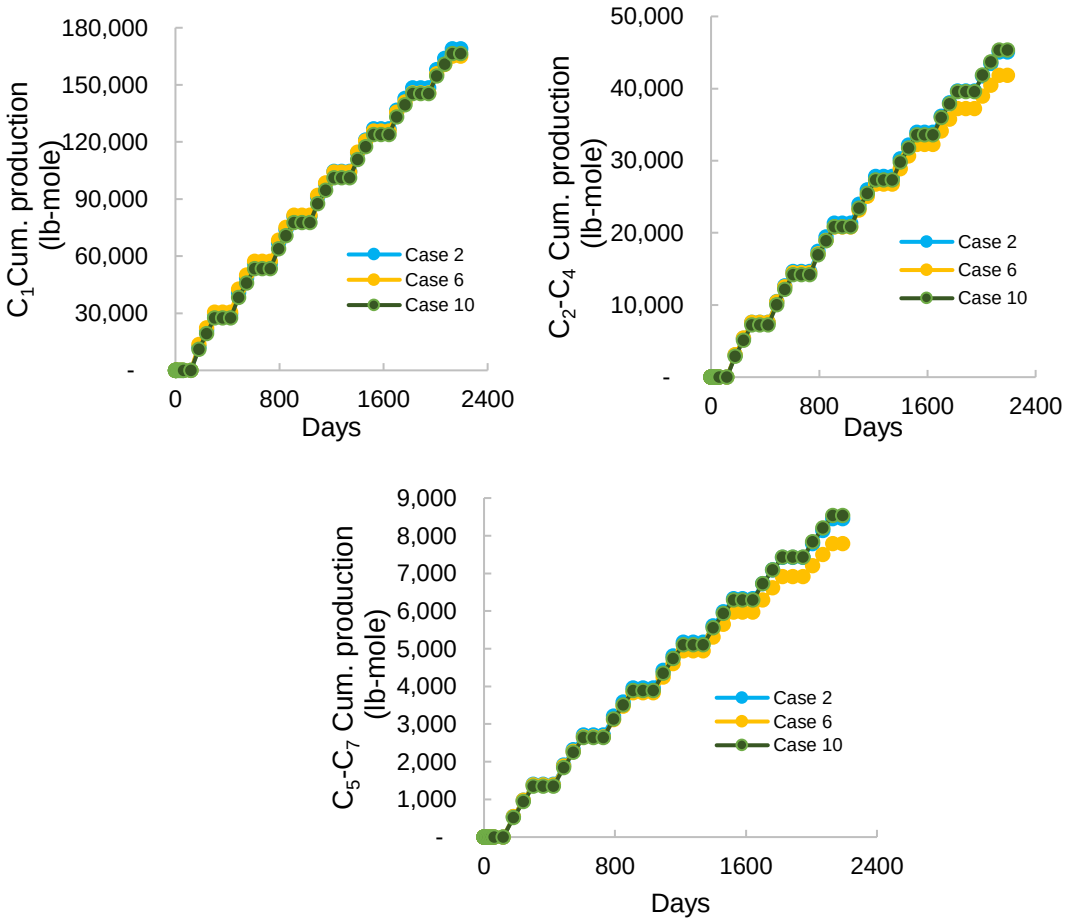


Figure 36. Component production stream (C_1, C_2-C_4, and C_5-C_7) comparison for different reservoir quality cases with diffusion effect.

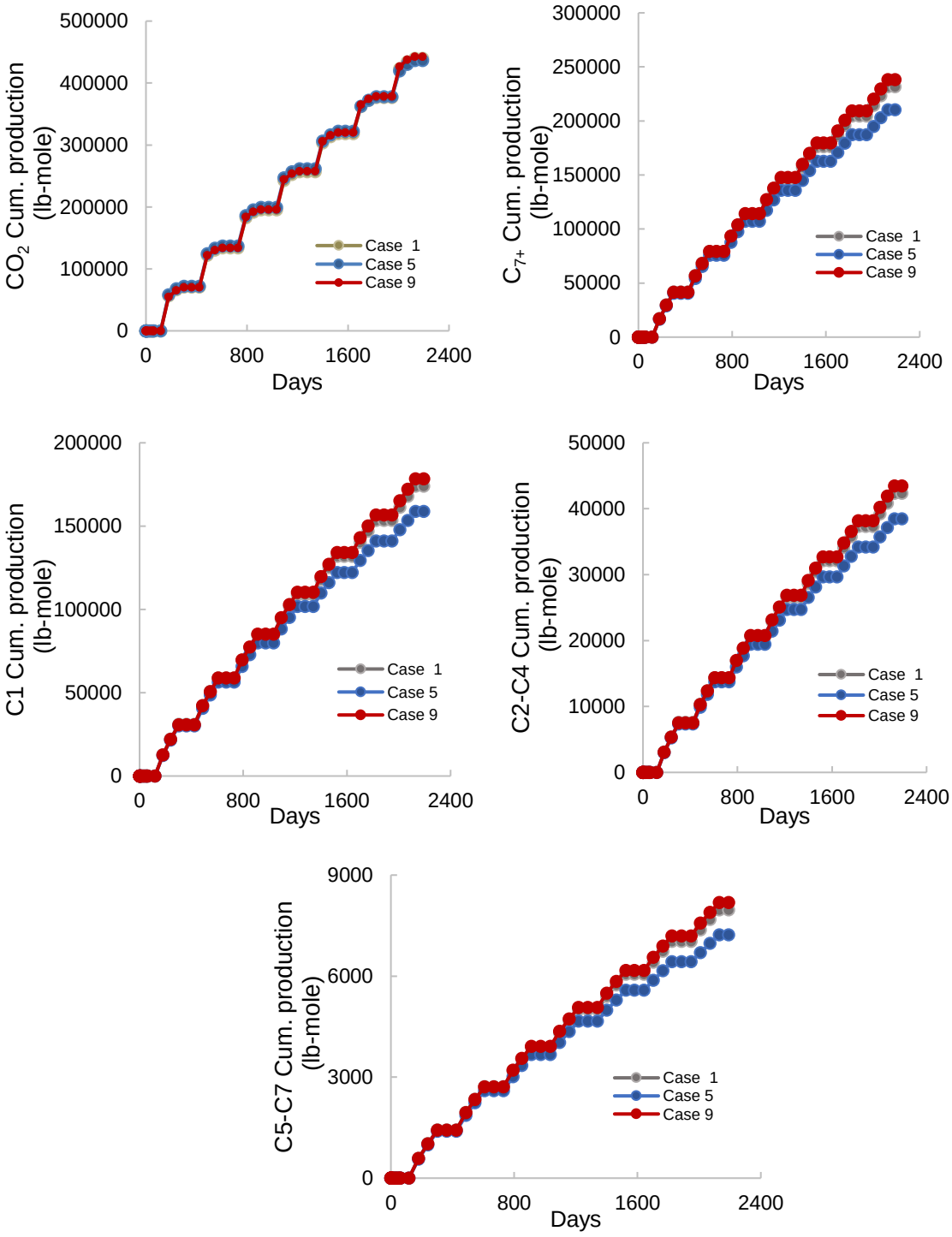


Figure 37. Component production stream (CO_2, C_{7+}, C_1, C_2-C_4, and C_5-C_7) comparison for different reservoir quality cases without diffusion effect.

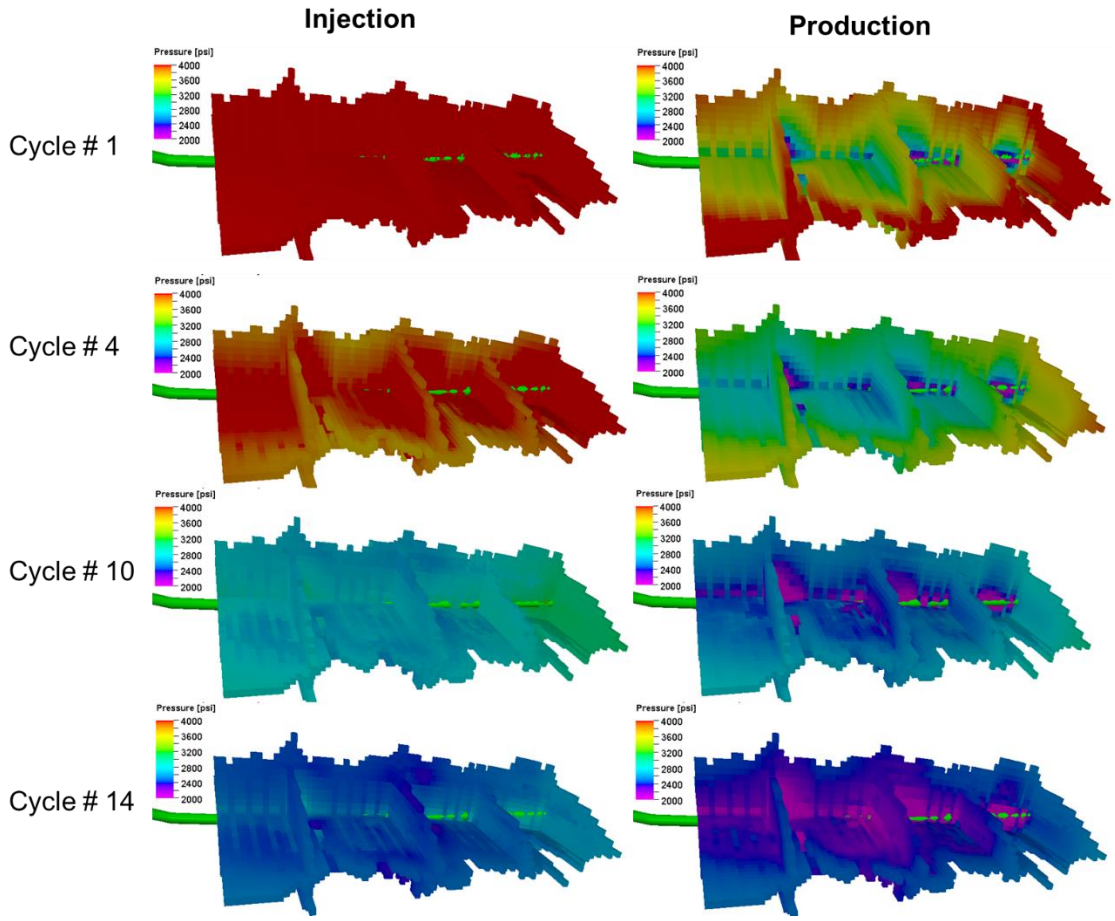


Figure 38. Pressure variation around the near wellbore regions through CO_2 huff-n-puff cycles

A2. Minimum Miscibility Pressure (MMP) Correlations

Metcalfe correlation:

$$MMP = 1833.717 + 2.2518055T + 0.01800674T^2 - \frac{103949.93}{T}$$

Where: T: reservoir temperature in ^{0}F

Cronquist correlation:

$$MMP = 15.988T^{0.744206+0.0011038M_{C5+}+0.0015279C_1}$$

Where: T: reservoir temperature in ^{0}F

M_{C5+}: molecular weight of C_{5+} components

C_1: mole percentage of C_1 component

Glaso correlation:

$$MMP = 810 - 3.404M_{C7+} + 1.7 \times 10^{-9} M_{C7+}^{3.73} e^{786.8M_{C7+}^{-1.058}} T \quad \text{where } C_{2-6} > 18\%$$

$$MMP = 2947.9 - 3.404M_{C7+} + 1.7 \times 10^{-9} M_{C7+}^{3.73} e^{786.8M_{C7+}^{-1.058}} T - 121.2C_{2-6}$$

where $C_{2-6} < 18\%$

Where: T: reservoir temperature in ^{0}F

M_{C7+}: molecular weight of C_{5+} components

C_{2-6}: mole percentage of C_{2-6} component

Yuan et al. correlation:

$$MMP = a_1 + a_2 M_{C7+} + a_3 C_{2-6} + \left(a_4 + a_5 M_{C7+} + a_6 \frac{C_{2-6}}{M_{C7+}}\right) T + (a_7 + a_8 M_{C7+} + a_9 M_{C7+}^2 + a_{10} C_{2-6}) T^2$$

Where: T: reservoir temperature in ^{0}F

M_{C7+}: molecular weight of C_{7+} components

C_{2-6}: mole percentage of C_{2-6} components

$a_1 = -1.4634E + 03$

$a_2 = 0.6612E + 01$

$a_3 = -4.4979E + 01$

$a_4 = 0.2139E + 01$

$a_5 = 1.1667E - 01$

$a_6 = 8.1661E + 03$

$a_7 = -1.2258E - 01$

$a_8 = -1.2883E - 03$

$a_9 = -4.0152E - 06$

$a_{10} = -9.2577E - 04$